NASA-CR-200251

INTERIM
NAG-2-CR
p-51

Progress Report
January 1996

Estimation of the Longitudinal and Lateral-Directional Aerodynamic Parameters from Flight Data for the NASA F/A-18 HARV

NASA Grant NCC 2-759

submitted by
Marcello R. Napolitano, Assistant Professor

G-60 Engineering Sciences Building
Department of Mechanical and Aerospace Engineering
West Virginia University
Morgantown, WV 26506/6106
Tel: (304)293-4111 Ext. 346
Fax: (304)293-8823
E-mail: napolit@cemr.wvu.edu

Technical Monitor:
Albion H. Bowers, Chief Research Engineer
NASA Dryden Flight Research Center
Edwards, CA 93523/0273
Tel: (805)258-3716

Abstract

This progress report presents the results of an investigation focused on parameter identification for the NASA F/A-18 HARV. This aircraft was used in the high alpha research program at the NASA Dryden Flight Research Center. In this study the longitudinal and lateral-directional stability derivatives are estimated from flight data using the Maximum Likelihood method coupled with a Newton-Raphson minimization technique. The objective is to estimate an aerodynamic model describing the aircraft dynamics over a range of angle of attack from 5° to 60°. The mathematical model is built using the traditional static and dynamic derivative buildup. Flight data used in this analysis were from a variety of maneuvers. The longitudinal maneuvers included large amplitude multiple doublets, optimal inputs, frequency sweeps and pilot pitch stick inputs. The lateral-directional maneuvers consisted of large amplitude multiple doublets, optimal inputs and pilot stick and rudder inputs. The parameter estimation code pEst, developed at NASA Dryden, was used in this investigation. Results of the estimation process from $\alpha = 5°$ to $\alpha = 60°$ are presented and discussed.

Table of Contents

Abstract 1

Table of Contents 2

Symbols 3

Introduction 4

Chapter 1: Maximum Likelihood Method and Newton Raphson Minimization 5

Chapter 2: Estimation of Longitudinal Aerodynamic Parameters

2.1 Mathematical Modeling of the Longitudinal Aircraft Dynamics 8

2.2 Estimation Procedures 10

2.3 Results of the Parameter Estimation Process 12

Chapter 3: Estimation of Lateral-Directional Aerodynamic Parameters

3.1 Mathematical Modeling of the Lateral-Directional Aircraft Dynamics 17

3.2 Estimation Procedures 19

3.3 Results of the Parameter Estimation Process 21

Chapter 4: Conclusions 26

References 27

List of Tables 28

List of Figure Captions 33

Symbols

a_n = normal acceleration, g
a_x = longitudinal acceleration, g
a_y = lateral acceleration, g
b = wing span, ft
$\overline{c}$ = mean aerodynamic chord, ft
C_i = aerodynamic coefficient where i=(N,m,A), rad^{-1} or deg^{-1}
E[ ] = expected value
g = gravity acceleration, ft/sec^2
I = moment of inertia, $slug\text{-}ft^2$
m = aircraft mass, slugs
p = roll rate, deg/sec
q = pitch rate, deg/sec
$\overline{q}$ = dynamic pressure, lbs/ft^2
R = conversion from radians to degrees (57.3)
r = yaw rate, deg/sec
S = wing planform area, ft^2
V = velocity, ft/sec
W/T = wind tunnel
x = sensor location, ft
y = computed aircraft response vector
z = measured aircraft response vector

Greek

α = angle-of-attack, deg
β = sideslip angle, deg
δ = control surface deflection, deg
θ = pitch attitude, deg
ξ = parameter vector to be estimated
Σ = summation
ϕ = roll attitude, deg
∇ = gradient

Subscripts

A = axial force
a = aileron
ba = basic airframe
D = drag force
dht = differential horizontal tail
e = elevator
L = lift force
l = rolling moment
lef = leading edge flap
m = pitching moment
N = normal force
n = yawing moment
pv = pitch vane
r = rudder
sa = symmetric aileron
t = true parameter value
tef = trailing edge flap
Y = lateral sideforce
yv = yaw vane

Introduction

The NASA High Alpha Technology Program (HATP) was initiated with the goal of obtaining a better understanding of aircraft aerodynamics, control surface effectiveness and airflow phenomena at high alpha flight conditions. Successful achievement of these goals are envisioned to allow expansion of flight envelopes, maneuverability enhancement and flight safety for future aircraft. The NASA F/A-18 High Alpha Research Vehicle (HARV) project is one of the flight test aircraft involved in this program.

The research work presented in this document is related to parameter identification (PID) for the HARV. The goal is to determine an aerodynamic model which accurately describes the dynamics of the HARV over a wide range of angle of attack conditions. This process allows the validation of wind tunnel data and results obtained from other PID methods. In addition, the development of a more accurate model is of great importance for updating flight simulators and onboard flight computers by enabling aircraft designers to better emulate the true system dynamics. Results from PID analysis may also be used as a tool for monitoring aircraft stability as well as control surface effectiveness while investigating the expansion of the flight envelope into the high alpha regime.

This report is related to the longitudinal and lateral-directional PID results for the HARV over a range from 5° to 60° for the angle of attack. The derivatives are extracted from flight data using the Maximum Likelihood (ML) method. The ML cost functional is maximized through the minimization of a quadratic cost function which contains the differences between measured and computed system responses. This minimization is achieved using the Newton-Raphson (NR) technique. The parameter estimation program (pEst), developed at NASA Dryden, is implemented in this research.

Flight data analyzed includes a variety of longitudinal and lateral-directional maneuvers obtained from the HARV flight testing activities. Particularly, the longitudinal maneuvers examined include single surface input multiple doublets (SSI MD), optimal longitudinal (OLON), 3211 frequency sweeps, and pilot pitch stick steps (PPSS). The lateral-directional flight data included single surface input multiple doublets (SSI MD), optimal lateral (OLAT) and pilot yaw/roll rudder and stick steps (PYRS) obtained from HARV.

Chapter1: Maximum Likelihood Method and Newton Raphson Algorithm

The ML method coupled with a NR minimization technique has been one of the most successful PID approaches for several years. The effectiveness of this approach is well documented and excellent results have been achieved for a large variety of aircraft, as presented in Refs. [1,2,4,5,7,8,9]. It is known that the estimates obtained using the ML method have three asymptotic properties: they are unbiased, approach a Gaussian distribution and have the lowest possible variance[6]. By asymptotic it implies that the aforementioned estimate properties are true if infinite data time is available. However, these estimate properties are best approximated if the data time is long enough (ie. a couple of periods of the lowest system natural frequency)[6]. In the case of an aircraft, "long enough" would be defined as a few periods of the phugoid mode.

In general, the objective is to maximize the probability that the computed system responses, based upon a set of estimated stability derivatives, are representative of the true system dynamics. This conditional probability, denoted as $P(z/\xi)$, is also known as the likelihood function. In this analysis it is assumed that all state and measurement noise may be described as a Gaussian, white sequence with zero mean. This allows the likelihood function to take on the following form:

$$P(z/\xi) = \frac{1}{2\pi^{\left(\frac{n_t n_z}{2}\right)} |W_1^{-1}|^{\frac{n_t}{2}}} \; e^{-J(\xi)} \qquad (1.1)$$

where the Gaussian probability density function $P(z/\xi)$ represents the ML cost functional to be maximized. Here W_1 represents the response error weighting matrix. The number of discrete time points in the maneuver and the number of responses in the cost function are denoted by n_t and n_z respectively. $J(\xi)$ represents the quadratic cost function to be minimized in order to maximize the likelihood function. This cost function is defined as follows:

$$J(\xi) = \frac{1}{2\, n_t\, n_z} \sum_{k=1}^{n_t} \left([z(t_k) - y(t_k)]^T W_1 [z(t_k) - y(t_k)] \right) \qquad (1.2)$$

By expressing $J(\xi)$ as its second order Taylor Series expansion and setting $\nabla_\xi J(\xi)$ equal to zero the NR technique generates an expression for updating the parameter vector at each iteration in the estimation process:

$$\xi_{i+1} = \xi_i - [(\nabla^2_\xi J(\xi_i))]^{-1} \nabla_\xi J(\xi_i) \qquad (1.3)$$

where the first gradient of $J(\xi_i)$ with respect to ξ is given by:

$$\nabla_{\xi} J(\xi_i) = \frac{-1}{n_t \, n_z} \sum_{k=1}^{n_t} \left[[\nabla_{\xi} y(t_k)]^T W_1 \, (z(t_k) - y(t_k)) \right] \tag{1.4}$$

The Gauss-Newton approximation of the second gradient of $J(\xi_i)$ with respect to ξ is as follows:

$$\nabla^2_{\xi} J(\xi_i) = \frac{1}{n_t \, n_z} \sum_{k=1}^{n_t} \left[[\nabla_{\xi} y(t_k)]^T W_1 \, \nabla_{\xi} y(t_k) \right] \tag{1.5}$$

A block diagram of the overall estimation procedure is shown in Figure 1. As illustrated, a predetermined set of control surface inputs are applied to the true aircraft system and the responses are recorded. The recorded control surface inputs and resulting aircraft responses are then read into the pEst code[3].

The aircraft mathematical model within pEst contains the polar coordinate form (α,β,V) of the 6 degree of freedom (DOF) non-linear aircraft equations of motion with the state equations being integrated using a fourth order Runge-Kutta numerical scheme. In addition, when computing estimated responses pEst also accounts for sensor locations with respect to the aircraft center of gravity (CG) to ensure that the cost function is comparing the same "local" responses recorded by the sensors. Most importantly, pEst is well-suited for user interaction allowing the analyst to determine which stability derivatives are to be estimated and which states or responses are to be included in the quadratic cost function. The user may also substitute measured flight data in place of those states or responses that are not computed within pEst. In addition, the diagonal weighting matrix (W_1) is easily set by the user to indicate which response errors are to be considered more important in the estimation procedure.

The recorded control inputs are then applied to the mathematical model of the aircraft within pEst and the differences between the measured and estimated responses are determined. The NR algorithm then determines the updated parameter vector to be used for the next iteration. This procedure continues until a desired convergence criteria for the change in the quadratic cost function $\Delta J(\xi)$ from one iteration to the next is met resulting in the final ML estimates of the aircraft model parameters.

The code is also capable of computing the corresponding Cramer-Rao bound for each derivative. This bound is a computed minimum standard deviation of the estimates which can be used as a measure of their goodness. With the assumption of asymptotically unbiased estimates the Cramer-Rao inequality may be written as:

$$\sigma(\hat{\xi}) = \sqrt{E[(\hat{\xi}-\xi_t)(\hat{\xi}-\xi_t)^T/\xi_t]} \geq \sqrt{M(\xi_t)^{-1}} \qquad (1.6)$$

The assumption of Gaussian, white system and measurement noise allows the Fisher information matrix $M(\xi_t)$ to be approximated as the Hessian of the quadratic cost function $J(\xi)$:

$$M(\xi_t) = \frac{1}{n_t\, n_z} \sum_{k=1}^{n_t} \left[[\nabla_\xi y(t_k)]^T W_1 \nabla_\xi y(t_k) \right] = \nabla^2_\xi J(\xi_t) \qquad (1.7)$$

This derivation is shown in Refs. [1,6]. In general, the most practical use of the Cramer-Rao bound is as a measure of scatter in the final estimates for the given flight data[6].

Chapter 2: Estimation of the Longitudinal Aerodynamic Parameters

2.1 Mathematical Modeling of the Longitudinal Aircraft Dynamics

Modeling of the aircraft longitudinal dynamics within pEst begins with the polar coordinate form (α,β,V) of the classical 6 DOF, non-linear equations of motion as seen in[4,9,11]. The body axis longitudinal equations of motion are shown below:

$$\dot{\alpha} = q - \tan\beta\,(p\cos\alpha + r\sin\alpha) - \frac{\bar{q}\,S\,R}{mV\cos\beta}C_L +$$

$$\frac{g\,R}{V\cos\beta}(\cos\theta\cos\phi\cos\alpha + \sin\theta\sin\alpha) - \frac{T\sin\alpha\,R}{mV\cos\beta} \qquad (2.1)$$

$$I_y\dot{q} - I_{yz}\dot{r} - I_{xy}\dot{p} = M_Y + [pr(I_z - I_x) + (r^2 - p^2)I_{xz} + qrI_{xy} - pqI_{yz}]\frac{1}{R} \qquad (2.2)$$

$$\dot{\theta} = q\cos\phi - r\sin\phi \qquad (2.3)$$

$$\dot{V} = -\frac{\bar{q}S}{m}C_D + g(\cos\phi\cos\theta\sin\alpha\cos\beta + \sin\phi\cos\theta\sin\beta -$$

$$\sin\theta\cos\alpha\cos\beta) + \frac{T}{m}\cos\alpha\cos\beta \qquad (2.4)$$

where :

$$C_L = C_N\cos(\alpha) - C_A\sin(\alpha) \qquad (2.5)$$

$$C_D = C_A\cos(\alpha) + C_N\sin(\alpha) \qquad (2.6)$$

In addition, adjustments were built into pEst to include the effects of angular rates and accelerations to the computed data to account for accelerometers which are non-coincident with the aircraft CG. The additional estimated parameters a_{nBias} and a_{xBias} are necessary to account for accelerometer instrumentation biases as shown:

$$a_n = \frac{\bar{q}S}{mg} C_N - \frac{1}{gR}\left[(x_{a_n} - x_{cg})\dot{q} + (y_{a_n} - y_{cg})\dot{p} \right] -$$

$$\frac{1}{gR^2}(z_{a_n} - z_{cg})(q^2 + p^2) + a_{nBias} \qquad (2.7)$$

$$a_x = -\frac{\bar{q}S}{mg} C_A - \frac{1}{gR}\left[(z_{a_x} - z_{cg})\dot{q} + (y_{a_x} - y_{cg})\dot{r} \right] +$$

$$\frac{1}{gR^2}(x_{a_x} - x_{cg})(q^2 + r^2) + a_{xBias} \qquad (2.8)$$

Similarly, the flow angle measurements for α recorded by the aircraft instrumentation are also affected by angular velocities and upwash if the flow vane is not coincident with the aircraft CG. Consequently, the computed flow angle α is adjusted within pEst as follows:

$$\alpha = k_\alpha \left[\alpha + (x_\alpha - x_{cg})\frac{q}{V} + (y_\alpha - y_{cg})\frac{p}{V} \right] \qquad (2.9)$$

Sensor and CG locations above, behind and to the right of the reference point are considered positive[3]. The reference point is located approximately 5 ft in front of the aircraft nose.

The linear buildups used to model the total, non-dimensional aerodynamic force and moment coefficients within pEst are given by:

$$C_N = C_{N_o} + C_{N_\alpha}\alpha + C_{N_{\delta e}}\delta e + C_{N_{\delta lef}}\delta lef + C_{N_{\delta tef}}\delta tef + C_{N_{\delta sa}}\delta sa +$$

$$\left(C_{N_{\delta pv}}\delta pv\right)\frac{1}{\bar{q}S} + C_{N_q}\left(\frac{\bar{c}}{2VR}\right)q \qquad (2.10)$$

$$C_m = C_{m_o} + C_{m_\alpha}\alpha + C_{m_{\delta e}}\delta e + C_{m_{\delta lef}}\delta lef + C_{m_{\delta tef}}\delta tef + C_{m_{\delta sa}}\delta sa + C_{m_q}\left(\frac{\bar{c}}{2VR}\right)q \qquad (2.11)$$

$$C_A = C_{A_o} + C_{A_\alpha}\alpha + C_{A_{\delta e}}\delta e + C_{A_{\delta lef}}\delta lef + C_{A_{\delta tef}}\delta tef + C_{A_{\delta sa}}\delta sa +$$

$$\left(C_{A_{\delta pv}}\delta pv\right)\frac{1}{\bar{q}S} + C_{A_q}\left(\frac{\bar{c}}{2VR}\right)q \qquad (2.12)$$

Note that the static buildup for the moment coefficient does not include the derivatives describing pitching moment effects due to the pitch vane. This moment derivative is found in the total pitching moment equation where:

$$M_Y = \bar{q}S\bar{c}C_m R - 6r(ERPM(I_{xe}))\frac{1}{R} + [C_{m_{\delta pv}}\delta pv]R \qquad (2.13)$$

The term ERPM represents engine revolutions per minute while I_{xe} denotes engine moment of inertia. The factor of 6 is simply a conversion from revolutions per minute to degrees per second. Note that a standard sign convention characterizing conventional control surface motion was employed: positive control surface deflection denoted as being trailing edge down. The overall pitch vane deflection was defined as positive for downward deflection of the exhaust plume.

2.2 Estimation Procedures

Four classes of longitudinal PID maneuvers were available for analysis in this effort. The SSI MD maneuvers consisted of independent longitudinal control surface doublets generated by OBES for the trailing-edge flaps, symmetrically deflected ailerons and the stabilator. The OLON runs included a series of 7.5° stabilator nose-up and nose-down pulses applied by OBES. The 3211 runs involved an OBES generated frequency sweep of the stabilator with a 7.5° amplitude of deflection. Such a maneuver consisted of four stabilator steps that alternate in sign with the first being three time units long, the second being two units in length and the last two pulses each being one time unit in duration. Each of the aforementioned maneuvers were performed with OBES on and the TVCS active. The PPSS runs, consisting of pilot pitch stick step inputs that alternate in sign, were divided into two subclasses: pilot pitch stick steps with the TVCS active (PPSSTV) and without (PPSS). Representative plots of the control surface inputs for the aforementioned maneuver types may be seen in Figure 2 recorded at an alpha of 20°. In each class of maneuver investigated, the longitudinal inputs were designed to minimize lateral-directional dynamics. All maneuvers were initiated under trimmed, straight and level flight conditions with all flight data sampled with a frequency of 40 Hz. The test maneuvers were performed with a fairly consistent CG location varying over the range of 24.5% - 26.7% $\bar{c}$.

Concerns regarding the possible instability and overestimation in magnitude of estimated derivatives due to high correlations in the flight data induced a need for model simplification. The presence of correlations among static and/or dynamic flight data implies that a dependency exists among them often leading to difficulties in extracting model parameters that describe their separate effects on the overall system. Such correlations often exist among control surface deflections which are dependently deployed with respect to other control surfaces, or other static flight data in the case of flight control system alpha scheduling. Analysis of the HARV flight data indicated that, under normal operating conditions, the leading-edge and trailing-edge flaps are deployed using a schedule imparting high correlations between each other, as well as angle of attack. The presence of this high correlation can clearly be seen in the sample time history of Figure 3a. To avoid biases in the derivative estimates all leading-edge flap derivatives ($C_{N\delta lef}$, $C_{m\delta lef}$ and $C_{A\delta lef}$) were held constant at their relative wind tunnel values during the estimation procedure. Similarly, all trailing-edge flap derivatives ($C_{N\delta tef}$, $C_{m\delta tef}$ and $C_{A\delta tef}$) were held constant at wind tunnel data for all maneuvers with the exception of those in which they were independently pulsed by OBES as in the case of the SSI MD maneuvers.

A similar technique was employed while analyzing the PPSSTV flight data in which high correlations between stabilator and pitch vane deflections, as can be seen in Figure 3b, were encountered due to a lack of independent control surface inputs. As a result, in an attempt to achieve more accurate estimates of the pitch vane coefficients, the stabilator derivatives ($C_{N\delta e}$, $C_{m\delta e}$ and $C_{A\delta e}$) were held constant at wind tunnel data during the estimation procedure. All wind tunnel values were based upon angle of attack and Mach for the maneuvers.

All mass properties (x_{cg}, y_{cg}, z_{cg}, I_x, I_y, I_z, I_{xz} and mass) were taken to be unique values for each individual maneuver investigated. These values were obtained from flight data with an average value of each property over the appropriate maneuver time being used in the mathematical model found in pEst. Finally, all lateral states and responses found in the aircraft equations of motion were replaced with measured flight data throughout the estimation process, as was the aircraft flight velocity V

This investigation produced a set of estimates for the following static and dynamic longitudinal derivatives for the NASA F/A-18 HARV: C_{No}, $C_{N\alpha}$, $C_{N\delta e}$, $C_{N\delta tef}$, $C_{N\delta pv}$, $C_{N\delta sa}$, C_{Nq}, C_{mo}, $C_{m\alpha}$, $C_{m\delta e}$, $C_{m\delta tef}$, $C_{m\delta pv}$, $C_{m\delta sa}$, C_{mq}, C_{Ao}, $C_{A\alpha}$, $C_{A\delta e}$, $C_{A\delta tef}$, $C_{A\delta pv}$, $C_{A\delta sa}$, C_{Aq}. In addition, the two parameters a_{nBias} and a_{xBias} were estimated

in order to model the measurement biases for the normal and axial linear accelerometers aboard the HARV. A complete listing of the estimated aerodynamic coefficients, as well as which derivatives were held constant at wind tunnel values, for each class of maneuver may be seen in Table 1.

In terms of the longitudinal cost function (J), the objective was to minimize the difference between the measured and computed values of α, q, θ, a_n and a_x as shown below:

$$J(\xi) = \frac{1}{2\ n_t\ n_z} \sum_{k=1}^{n_t} \left(\begin{bmatrix} \alpha(t_k) - \hat{\alpha}(t_k) \\ q(t_k) - \hat{q}(t_k) \\ \theta(t_k) - \hat{\theta}(t_k) \\ a_n(t_k) - \hat{a}_n(t_k) \\ a_x(t_k) - \hat{a}_x(t_k) \end{bmatrix}^T \begin{bmatrix} A & 0 & 0 & 0 & 0 \\ 0 & B & 0 & 0 & 0 \\ 0 & 0 & C & 0 & 0 \\ 0 & 0 & 0 & D & 0 \\ 0 & 0 & 0 & 0 & E \end{bmatrix} \begin{bmatrix} \alpha(t_k) - \hat{\alpha}(t_k) \\ q(t_k) - \hat{q}(t_k) \\ \theta(t_k) - \hat{\theta}(t_k) \\ a_n(t_k) - \hat{a}_n(t_k) \\ a_x(t_k) - \hat{a}_x(t_k) \end{bmatrix} \right) \qquad (2.13)$$

where the terms α, q, θ, a_n and a_x are the responses measured from the aircraft. The corresponding responses computed in pEst are denoted by $\hat{\alpha}$, $\hat{q}$, $\hat{\theta}$, $\hat{a}_n$ and $\hat{a}_x$. The diagonal matrix within the cost function represents the user defined weighting matrix (W_1). A trial and error approach was used to determine the best set of weightings for each class of maneuver investigated. A listing of the A, B, C, D and E elements of the weighting matrix, as was used for each class of maneuver, is given in Table 2.

2.3 Results of the Parameter Estimation Process

The results of the investigation are in terms of comparisons of actual and calculated time histories as well as estimates of the longitudinal derivatives and a comparison with the wind tunnel estimates. Although estimates were obtained for the C_N, C_m and C_A derivative subcomponents this paper emphasizes the subcomponents of C_N and C_m only. This is due to the fact that the maneuvers under investigation did not adequately excite axial acceleration (a_x) or aircraft flight velocity enough to obtain confident estimates of the axial coefficients.

An analysis of the actual and calculated time histories reveals that, overall, the minimization technique has resulted in an accurate representation of the measured HARV responses even at higher angles of attack. A typical sample time history match may be seen in Figure 4 showing time history comparisons between measured and computed α, q, θ and a_n responses at 30° alpha for the SSI MD class maneuver. Of course, accurate fits between

measured and computed aircraft responses does not alone imply that an accurate aerodynamic model has been estimated.

The final PID results for the main longitudinal static and dynamic parameters are shown in Figures 5-7 related to an angle of attack range of 5°- 60°. Each estimate in the plots indicate the maneuver type spawning that estimate as well as its Cramer-Rao bound graphically represented as a vertical bar. Recall that the Cramer-Rao bounds are equivalent to an estimated minimum standard deviation for a given estimate which, ideally, should accurately describe the scatter of the estimates at each angle of attack[6]. Some considerations are needed for a better understanding of results in terms of the Cramer-Rao bounds. In fact, recall that the determination of the Cramer-Rao bounds assumes unbiased estimates with system and measurement noise being described as a Gaussian, white sequence. Considering a case where these assumptions are truly valid the time history residuals would also be white, random sequences resulting in a set of Cramer-Rao bounds accurately modeling the scatter of the estimates. However, such ideal test conditions are only guaranteed if flight data obtained through computer simulation is being investigated. As expressed in Ref. [6], analysis of real flight data may result in biased estimates often caused by modeling inadequacies or poor system excitation. Furthermore, colored system or measurement noise will also affect the computed residuals. As a result, in the case of residuals correlated in this manner, optimistically underestimated Cramer-Rao bounds are often calculated causing an inadequate model for the scatter of the estimates.

A variety of techniques to "correct" the Cramer-Rao bounds are discussed in detail in Ref. [6]. One such technique involves multiplying the bounds by a factor, often 5-10, to compensate for the effects of the colored residuals. A more precise method in Ref. [6] is based on the determination of a unique correction multiplier for each Cramer-Rao bound through examination of the power spectral density for the response residuals generated by the estimates. Note that the Cramer-Rao bounds presented herein are not adjusted.

In order to compare the coefficient estimates with the corresponding values obtained from wind tunnel tests an important distinction between the wind tunnel model and the estimated HARV parameters had to be made. The tunnel database models a "basic airframe" normal force coefficient (C_{N_ba}) which represents the linear combination of the normal force aerodynamic bias (C_{N_o}) and the effect of the lift curve slope. Similarly, a "basic airframe" moment coefficient (C_{m_ba}) is presented which involves a linear combination of pitching moment aerodynamic bias

(C_{mo}) with the effects of the pitching moment coefficient due to alpha. These coefficient representations used in the wind tunnel modeling are shown below:

$$C_{N\_ba} = C_{N_o} + C_{N_\alpha}\alpha \qquad (2.14)$$

$$C_{m\_ba} = C_{m_o} + C_{m_\alpha}\alpha \qquad (2.15)$$

All other model parameters were compatible for straight forward comparison with the estimated HARV derivatives with the exception of the thrust vectoring control derivatives for which, of course, aerodynamic wind tunnel data were not available. Since the estimated coefficients of C_{No}, $C_{N\alpha}$, C_{mo} and $C_{m\alpha}$ were not directly presented in the tunnel database these estimates were combined in the aforementioned manner to present the estimated "basic airframe" normal force and moment coefficients for the HARV.

The estimates of the normal force coefficients are shown in the left side of Figures 5-7. In general, the normal force coefficients were determined with consistency at each angle of attack with clear trends over the entire alpha range. In addition, the Cramer-Rao bounds closely model the scatter achieved by some of the estimates, especially at lower angles of attack. However, many of the bounds show evidence of underestimation. Overall, it is clear that each flight maneuver tested is equally capable of concisely estimating most of the normal force coefficients. However, there are two main exceptions to this conclusion. Examination of the estimates for $C_{N\delta pv}$ in Figure 7 clearly indicates that the PPSSTV maneuvers, analyzed with all elevator derivatives held constant to wind tunnel values, result in more consistent estimates over the entire alpha range. The estimates for the normal force coefficient due to pitch rate (C_{Nq}) in Figure 7 also show that the PPSS and PPSSTV maneuvers yield more consistent results with very little scatter over the range of alpha investigated. The SSI MD maneuver results, on the other hand, indicate considerable scattering in this estimate. This is not surprising since the pilot inputs of the PPSS and PPSSTV class maneuvers involve much more sustained excitation in pitch rate than those of the SSI MD OBES inputs as shown in Figure 8.

The results for the estimates of the pitching moment coefficients do not show, in general, the same consistency found in the estimates of the normal force coefficients although most estimates still indicate a detectable trend. In fact, the results show a severe scatter of the estimates, particularly at high angles of attack. However,

closer examination indicates that the majority of the scatter in these coefficients is due to the estimates obtained using the SSI MD maneuver data. In fact, it appears that the pitching moment estimates found through analysis of the PPSS and PPSSTV data are much more consistent at each angle of attack. This is especially evident in the estimates for C_{mq} and $C_{m\delta pv}$. Again, this may be due to the highly sustained pitch rate excitation produced by these maneuver types.

The PID estimates for C_{N_ba} show good consistency with the wind tunnel data at low angles of attack. At higher values of alpha the overall "basic airframe" normal force estimates are lower than the corresponding tunnel data. The consistency and low scattering present in the C_{No} and $C_{N\alpha}$ estimates may suggest that the estimates from flight data are more realistic than the wind tunnel predicted values. The "basic airframe" pitching moment estimates (C_{m_ba}) also indicate a close match with the tunnel data at lower alphas. However, again there is a substantial scatter in the estimates at higher angles of attack. The consistent estimates from the PPSSTV maneuver indicate a higher negative basic airframe pitching moment than was predicted by the wind tunnel tests at higher alphas. Comparisons between PID estimates and wind tunnel data for the elevator normal force ($C_{N\delta e}$) and moment coefficients ($C_{m\delta e}$) are also shown in Figure 5. Overall, the trends of these estimates match the trend relative to wind tunnel data. However, estimates for $C_{N\delta e}$ at $\alpha = 40°$ are consistently of lower magnitude than the wind tunnel data.

The estimated normal force and moment coefficients for symmetric ailerons ($C_{N\delta a}$, $C_{m\delta a}$) and trailing edge flaps ($C_{N\delta tef}$, $C_{m\delta tef}$) are compared to wind tunnel data in Figure 6. There is only a limited agreement between the PID estimates and the wind tunnel estimates.

Figure 7 shows instead the estimates of the normal force and pitching moment coefficients associated with the pitch vanes of the thrust vectoring system ($C_{N\delta pv}$, $C_{m\delta pv}$) as well as the dynamic coefficients pertaining to pitch rate (C_{Nq}, C_{mq}). Among the longitudinal maneuvers, the PPSSTV maneuvers, performed with OBES off and the TVCS on, were particularly effective in extracting estimates for $C_{N\delta pv}$ and $C_{m\delta pv}$ which reveal a clear and precise trend with limited scatter as opposed to the other maneuvers analyzed. The trend is made more noticeable by the least squares fits shown in the top of Figure 7 which were generated using PPSSTV estimates only. The results for C_{Nq} and C_{mq} may again be seen in the bottom of Figure 7. As previously mentioned, the estimates for C_{Nq} and C_{mq} resulting from analysis of the PPSS and PPSSTV maneuvers are much more consistent over the entire alpha range

tested with very little scatter. Consequently, the least squares fits shown on these plots were generated using the PPSS and PPSSTV estimates only. Overall, flight tests indicate a much higher normal force due to pitch rate than was predicted during wind tunnel tests. Similarly, the least squares fit for the PPSS and PPSSTV data indicate a trend for pitch damping (C_{mq}) that is slightly higher in magnitude than that predicted by the wind tunnel data.

Chapter 3: Estimation of the Lateral-Directional Aerodynamic Parameters

3.1 Mathematical Modeling of the Aircraft Dynamics

Modeling of the aircraft lateral dynamics begins with the polar coordinate form (α,β,V) of the classical 6 DOF, non-linear equations of motion shown in Refs. [9,11]. The body axis lateral-directional equations of motion are given by:

$$\dot{\beta} = p\sin\alpha - r\cos\alpha + \frac{\bar{q}sR}{mV} C_{Ywind} + \frac{gR}{V}(\cos\beta\cos\theta\sin\phi) +$$

$$\frac{gR}{V}(-\sin\beta(\cos\theta\cos\phi\sin\alpha - \sin\theta\cos\alpha)) + \frac{TR}{mV}\cos\alpha\sin\beta \qquad (3.1)$$

$$I_x\dot{p} - I_{xy}\dot{q} - I_{xz}\dot{r} = M_X + [qr(I_y - I_z) + (q^2 - r^2)I_{yz} + pqI_{xz} - prI_{xy}]\frac{1}{R} \qquad (3.2)$$

$$I_z\dot{r} - I_{xz}\dot{p} - I_{yz}\dot{q} = M_Z + [pq(I_x - I_y) + (p^2 - q^2)I_{xy} + prI_{yz} - qrI_{xz}]\frac{1}{R} \qquad (3.3)$$

$$\dot{\phi} = p + \tan\theta(r\cos\phi + q\sin\phi) \qquad (3.4)$$

where :

$$C_{Ywind} = C_Y\cos\beta + C_D\sin\beta \qquad (3.5)$$

$$C_D = C_A\cos(\alpha) + C_N\sin(\alpha) \qquad (3.6)$$

In addition, adjustments were built into pEst to include the effects of angular rates and accelerations on the computed data to account for accelerometers which are non-coincident with the aircraft CG. The additional estimated parameter $a_{y_{Bias}}$ is necessary to account for the accelerometer instrumentation bias as shown:

$$a_y = \frac{\bar{q}S}{mg} C_Y + \frac{1}{gR}\left[-(x_{a_y}-x_{cg})\dot{r}+(z_{a_y}-z_{cg})\dot{p}\right] - \frac{1}{gR^2}(y_{a_y}-y_{cg})(p^2+r^2) + a_{yBias} \quad (3.7)$$

Similarly, the flow angle measurements for β recorded by the aircraft instrumentation are also affected by angular velocities and sidewash if the flow vane is not coincident with the aircraft CG. Consequently, the computed flow angle β is adjusted within pEst as follows:

$$\beta = k_\beta\left[\beta+(z_\beta-z_{cg})\frac{p}{V}-(x_\beta-x_{cg})\frac{r}{V}\right] \quad (3.8)$$

Sensor and CG locations above, behind and to the right of the reference point are considered positive[3]. The reference point is located approximately 5 ft in front of the aircraft nose.

The linear buildup used to model the total, non-dimensional aerodynamic force and moment coefficients within pEst are as follows:

$$C_Y = C_{Y_o} + C_{Y_\beta}\beta + C_{Y_{\delta a}}\delta a + C_{Y_{\delta dht}}\delta dht + C_{Y_{\delta r}}\delta r +$$

$$\left(C_{Y_{\delta yv}}\delta yv\right)\frac{1}{\bar{q}S} + C_{Y_p}\left(\frac{b}{2VR}\right)p + C_{Y_r}\left(\frac{b}{2VR}\right)r \quad (3.9)$$

$$C_l = C_{l_o} + C_{l_\beta}\beta + C_{l_{\delta a}}\delta a + C_{l_{\delta dht}}\delta dht + C_{l_{\delta r}}\delta r +$$

$$C_{l_p}\left(\frac{b}{2VR}\right)p + C_{l_r}\left(\frac{b}{2VR}\right)r \quad (3.10)$$

$$C_n = C_{n_o} + C_{n_\beta}\beta + C_{n_{\delta a}}\delta a + C_{n_{\delta dht}}\delta dht + C_{n_{\delta r}}\delta r +$$

$$C_{n_p}\left(\frac{b}{2VR}\right)p + C_{n_r}\left(\frac{b}{2VR}\right)r \quad (3.11)$$

It should be noted that the static buildup for the rolling and yawing moment coefficients do not include the derivatives modeling moment effects due to yaw vane deflections. These moment derivatives are found in the total rolling and yawing moment equations:

$$M_X = \bar{q}SbC_l R + [C_{l_{\delta yv}} \delta yv]\, R \tag{3.12}$$

$$M_Z = \bar{q}SbC_n R + 6q(ERPM(I_{xe}))\,\frac{1}{R} + [C_{n_{\delta yv}} \delta yv]\, R \tag{3.13}$$

The second term on the right side of Eq. (3.13) is related to the gyroscopic effects of the engines. The term ERPM denotes engine revolutions per minute and I_{xe} represents the moment of inertia of the engines. The factor of 6 is simply a conversion factor from revolutions per minute to degrees per second. A standard sign convention for control surface deflection was employed: positive rolling control surface deflections induce a positive roll rate, positive rudder deflection is defined as trailing edge left. The overall yaw vane deflection was considered positive for deflection of the exhaust plume to the right.

3.2 Estimation Procedures

Three types of lateral maneuvers were available for PID purposes. The SSI MD maneuvers consisted of independent lateral control surface doublets generated by the On Board Excitation System (OBES) for the ailerons, differential horizontal tail, rudder, and yaw vanes. The OLAT runs included a series of 5° aileron and 10° rudder doublets applied by OBES. Recall that the OBES is instrumental in generating the independent control surface deflections necessary for more accurate estimates by minimizing correlated control surface inputs. Each of the previous maneuvers were performed by the OBES with the TVCS active. The PYRS maneuvers, which were not executed using OBES, were separated into two subclasses: pilot yaw/roll steps without thrust vectoring (PYRS) and with thrust vectoring (PYRSTV). The PYRS maneuvers consisted of a series of 1.5" rudder steps followed by a series of 2.5" lateral stick steps both alternating in sign. The PYRSTV inputs consisted of 1.5" rudder steps followed by 1.5" lateral stick steps of alternating sign. Representative plots of the control surface inputs for the maneuver types described above may be seen in Figure 9 recorded at an alpha of 20°. For each maneuver class, the lateral inputs were designed to minimize longitudinal dynamic responses. All maneuvers were initiated under trimmed, straight and level flight conditions with all flight data sampled with a frequency of 40 Hz.

Concerns regarding a possible dynamic instability and overestimation in magnitude of estimated derivatives

due to correlations in the flight data induced a need for a model simplification. The presence of correlation among static and/or dynamic flight data implies that a dependency exists among them often leading to difficulties in extracting model parameters that describe their separate effects on the overall system. These correlations often exist among control surface deflections which are dependently deployed with respect to one another. An analysis of the HARV lateral flight data for the PYRS maneuver clearly indicates a high correlation between aileron and differential horizontal tail inputs when the standard flight control system is active. There is also a dependency between roll and yaw control inputs applied by the aileron-rudder interconnect (ARI) of the standard F/A-18 flight control system. These highly correlated inputs are clearly indicated in Figure 10. As a result, all differential horizontal tail derivatives ($C_{Y\delta dht}$, $C_{l\delta dht}$ and $C_{n\delta dht}$) were held constant at wind tunnel values during the analysis of the PYRS data so that more accurate aileron coefficients could be obtained. The operation of the ARI during these pilot yaw/roll step maneuvers threatened to introduce difficulties in extracting the cross-coupling control derivatives $C_{Y\delta a}$, $C_{n\delta a}$ and $C_{l\delta r}$. Analysis of the PYRS maneuvers at 20° angle of attack achieved best results when these cross-coupling control derivatives were held constant at the estimates from wind tunnel analysis. However, PYRS data analysis at 30° angle of attack and higher required that only the cross-coupling control derivative $C_{n\delta a}$ be held constant at appropriate wind tunnel values.

Similarly, examination of the PYRSTV flight data also indicates a high correlation between aileron and differential horizontal tail inputs as well as a dependency between roll and yaw control inputs applied by the ARI of the standard F/A-18 flight control system. In addition, when the TVCS is active there is an additional correlation between rudder and yaw vane inputs. A sample time history showing these correlations may be seen in Figure 11. Best results were obtained during the analysis of the PYRSTV flight data by holding all differential horizontal tail derivatives ($C_{Y\delta dht}$, $C_{l\delta dht}$ and $C_{n\delta dht}$) as well as all rudder coefficients ($C_{Y\delta r}$, $C_{l\delta r}$ and $C_{n\delta r}$) constant at appropriate wind tunnel values in order to obtain better estimates for the aileron and yaw vane derivatives. All wind tunnel values were based upon angle of attack and Mach for the maneuvers.

All mass properties (x_{cg}, y_{cg}, z_{cg}, I_x, I_y, I_z, I_{xz} and mass) were taken to be unique values for each individual maneuver. These values were obtained from flight data with an average value over the appropriate maneuver time being used in the mathematical model found in pEst. Finally, all longitudinal states and responses found in the

aircraft equations of motion, including the aircraft flight velocity V, were replaced with measured flight data throughout the estimation process.

The following static and dynamic lateral-directional derivatives were estimated for the NASA F/A-18 HARV: C_{Y_o}, $C_{Y\beta}$, $C_{Y\delta a}$, $C_{Y\delta dht}$, $C_{Y\delta r}$, $C_{Y\delta yv}$, C_{Yp}, C_{Yr}, C_{lo}, $C_{l\beta}$, $C_{l\delta a}$, $C_{l\delta dht}$, $C_{l\delta r}$, $C_{l\delta yv}$, C_{lp}, C_{lr}, C_{no}, $C_{n\beta}$, $C_{n\delta a}$, $C_{n\delta dht}$, $C_{n\delta r}$, $C_{n\delta yv}$, C_{np}, C_{nr}. The additional parameter $a_{y_{Bias}}$ was estimated in order to model the measurement bias for the lateral accelerometer aboard the HARV. A complete listing of which aerodynamic coefficients were estimated, as well as which derivatives were held constant at wind tunnel values, for each class of maneuver may be seen in Table 3.

In terms of the lateral-directional cost function (J), the objective was to minimize the difference between the measured and computed values of β, p, r, ϕ and a_y as shown below.

$$J(\xi) = \frac{1}{2\, n_t\, n_z} \sum_{k=1}^{n_t} \left(\begin{bmatrix} \beta(t_k) - \hat{\beta}(t_k) \\ p(t_k) - \hat{p}(t_k) \\ r(t_k) - \hat{r}(t_k) \\ \phi(t_k) - \hat{\phi}(t_k) \\ a_y(t_k) - \hat{a}_y(t_k) \end{bmatrix}^T \begin{bmatrix} A & 0 & 0 & 0 & 0 \\ 0 & B & 0 & 0 & 0 \\ 0 & 0 & C & 0 & 0 \\ 0 & 0 & 0 & D & 0 \\ 0 & 0 & 0 & 0 & E \end{bmatrix} \begin{bmatrix} \beta(t_k) - \hat{\beta}(t_k) \\ p(t_k) - \hat{p}(t_k) \\ r(t_k) - \hat{r}(t_k) \\ \phi(t_k) - \hat{\phi}(t_k) \\ a_y(t_k) - \hat{a}_y(t_k) \end{bmatrix} \right) \qquad (3.14)$$

Here the terms β, p, r, ϕ and a_y are the responses measured from the aircraft while the corresponding responses computed in pEst are denoted by $\hat{\beta}$, $\hat{p}$, $\hat{r}$, $\hat{\phi}$ and $\hat{a}_y$. The diagonal matrix within the cost function represents the user defined weighting matrix (W_1). A trial and error approach was used to determine the best set of weightings for each class of maneuver investigated. A listing of the A, B, C, D and E elements of the weighting matrix, as was used for each class of maneuver, may be seen in Table 4

3.3 Results of the Parameter Estimation Process

The results for the lateral-directional stability derivatives of the NASA F/A-18 HARV are presented in terms of time history comparisons between measured and computed aircraft responses as well as estimates for the aerodynamic coefficients which are shown in comparison with wind tunnel data. Overall, estimates were obtained for the aerodynamic subcomponents of the total roll, yaw and side force coefficients (C_l, C_n and C_Y).

Comparison between computed aircraft responses, generated using the estimated aerodynamic model, and measured time histories indicate that an accurate representation of the HARV lateral-directional flight data responses have been obtained even at higher alphas. Figure 12 offers a representative sample of the most important time history fits of β, p, r and ϕ at an alpha of 30° for the SSI MD class maneuver.

Estimation results for the main lateral-directional stability derivatives are presented in Figures 13-16 over a flight regime of 5°- 60° angle of attack. Each estimate is shown with its corresponding Cramer-Rao bound represented graphically as a vertical bar. Recall that the Cramer-Rao bound is a computed lower bound of the standard deviation of each estimate which, under ideal estimation conditions, should accurately model the scatter of the estimates at each angle of attack[6]. Some considerations are needed for a better understanding of results in terms of the Cramer-Rao bounds. In fact, recall that the determination of the Cramer-Rao bounds assumes unbiased estimates with system and measurement noise being described as a Gaussian, white sequence. Considering a case where these assumptions are truly valid the time history residuals would also be white, random sequences resulting in a set of Cramer-Rao bounds accurately modeling the scatter of the estimates. However, such ideal test conditions are only guaranteed if flight data is obtained through computer simulation. As expressed in Ref. [6], analysis of real flight data may result in biased estimates often caused by modeling inadequacies or poor system excitation. Furthermore, colored system or measurement noise will also affect the computed residuals. As a result, in the case of residuals correlated in this manner, optimistically underestimated Cramer-Rao bounds are often calculated causing an inadequate model for the scatter of the estimates.

A variety of techniques to "correct" the Cramer-Rao bounds are discussed in Ref. [6]. One such technique involves multiplying the bounds by a factor, often 5-10, to compensate for the effects of the colored residuals. A more precise method discussed in Ref. [6] entails determining a unique correction multiplier for each bound through examination of the power spectral density for the response residuals generated by the estimates. Note that the Cramer-Rao bounds presented herein are not adjusted.

Overall, estimates of the static derivatives show good consistency with well defined trends. In addition, some of the Cramer-Rao bounds are successful in modeling the estimate scatter at the lower angles of attack. However, the majority of the bounds are clearly underestimated.

An interesting trend was determined, as seen in Figure 13, for the dihedral effect ($C_{l\beta}$) in which the estimates start at a low magnitude at an angle of attack of approximately 5°-10° and clearly increase to a maximum magnitude at about 20° alpha. The magnitude of the dihedral effect decreases steadily thereafter. The results for the aircraft yawing coefficient due to sideslip ($C_{n\beta}$) indicate that the HARV is directionally stable in yaw with $C_{n\beta}$ positive up to approximately 30° angle of attack. However, estimates indicate that the aircraft becomes unstable in yaw at alpha $>30°$, as is indicated with $C_{n\beta}$ being negative.

Figures 13-14 indicate an expected degradation in the rolling effectiveness of the ailerons ($C_{l\delta a}$) and differential stabilizer ($C_{l\delta dht}$) as the angle of attack increases. This may be due to slow speeds and flow separation which occur under high alpha flight conditions. Similarly, as seen in Figure 14, the yaw control of the rudder ($C_{n\delta r}$) was found to become less efficient at higher angles of attack. This could be caused, most likely, by the rudder being in the wake of a highly turbulent, separated airflow from the wing under such flight conditions. Although the estimates for the cross-coupling control derivatives ($C_{n\delta a}$, $C_{n\delta dht}$ and $C_{l\delta r}$) do not show the same consistency as the primary control derivatives ($C_{l\delta a}$, $C_{l\delta dht}$ and $C_{n\delta r}$) a clear trend is still indicated. Finally, as it can be seen in Figure 16, the yaw control effectiveness of the thrust vectoring vanes ($C_{n\delta yv}$) aboard the HARV remains almost constant over the entire flight regime with only a slight variation in magnitude.

The main lateral-directional side force coefficient estimates with the most defined trends may also be seen in Figure 16. Again, the majority of the scatter is obtained at higher alphas with the estimates for the SSI MD maneuvers. As expected, the side force effectiveness of the yaw vanes ($C_{Y\delta yv}$) remains nearly constant over the entire flight regime investigated. The results for the side force effectiveness of the rudder ($C_{Y\delta r}$) indicate a loss of rudder effectiveness as alpha increases. In addition, the scatter in the estimates for $C_{Y\delta r}$ at higher alphas indicate a possible rudder control reversal under these flight conditions. However, such a control reversal is clearly not present in the rudder yaw control results for the $C_{n\delta r}$ estimates previously examined in Figure 14.

Among the dynamic coefficients estimated, the most consistent results were obtained for C_{lp} and C_{nr} as can be seen in Figure 15. Overall, these coefficients indicate a damping effect against roll and yaw respectively. The majority of the scattered dynamic derivative estimates are represented by results obtained using the OLAT inputs. This may be due to a lack of proper excitation in roll and yaw resulting from the OLAT maneuvers in the estimation

of these coefficients. In addition, some scatter of the SSI MD estimates is present at higher alphas.

A comparison between the main lateral-directional aerodynamic estimates from flight data with the corresponding values in the NASA F/A-18 HARV wind tunnel database was also conducted. These final comparisons may also be seen in Figures 13-16. Each plot contains a least squares curve fit which has been generated through the estimates for comparison with the appropriate wind tunnel values when available. Note that the F/A-18 wind tunnel database does not include values that are directly comparable to $C_{l\beta}$, $C_{n\beta}$ and $C_{Y\beta}$. In fact, the wind tunnel data linearly combines the effects of each sideslip coefficient with the appropriate roll, yaw or sideforce aerodynamic bias coefficient into one overall term. In addition, no compatible wind tunnel data was available for direct comparison with the yaw vane coefficient estimates.

Figure 13 shows a comparison between the estimates, and corresponding tunnel data, for the rolling and yawing coefficients due to aileron deflection ($C_{l\delta a}$ and $C_{n\delta a}$). The estimates for $C_{l\delta a}$ are in close accordance with the listed tunnel data whereas the results for $C_{n\delta a}$ are consistently lower in magnitude than the tunnel data. This trend indicates less adverse yaw than expected due to aileron deflection at higher angles of attack.

Comparisons for the rudder roll and yaw estimates are presented in Figure 14. The estimates for $C_{n\delta r}$ match the tunnel data with good accuracy. However, estimates for adverse roll due to rudder deflection ($C_{l\delta r}$) are close to wind tunnel estimates at the low and high ends of the flight regime between 10°- 60° alpha. In the region of 30°- 40° alpha the estimates for $C_{l\delta r}$ are consistently higher than those available in the wind tunnel database.

Estimates for $C_{l\delta dht}$, as seen in Figure 14, are consistently higher than those of the wind tunnel data. Similarly, resulting estimates for $C_{n\delta dht}$ show that, as angle of attack increases, the flight data indicate a higher magnitude of adverse yaw due to differentially deflected stabilizers than was previously modeled in the wind tunnel database.

The least squares fit of the dynamic coefficient estimates of C_{lp} and C_{nr} are shown in Figure 15. Both fits show good agreement with the wind tunnel data. Similar results were obtained for the least squares fits of the dynamic coefficient estimates of C_{lr} and C_{np}.

Comparisons of the estimates for $C_{Y\delta r}$ with wind tunnel data may be seen in Figure 16. Again, the least squares fit through the estimates agrees with the wind tunnel values, especially at low angles of attack. However,

closer examination shows that for $\alpha \geq 40°$ a major divergence from the wind tunnel data is encountered in which the flight data indicates a possible rudder control reversal. Again, this control reversal was not indicated by the $C_{n\delta r}$ estimates.

Chapter 4: Conclusions

This paper has presented the longitudinal and lateral-directional stability and control derivatives obtained for the NASA F/A-18 HARV from flight data using the Maximum Likelihood estimation technique with a Newton-Raphson minimization scheme over a flight regime of 5° - 60° angle of attack. The mathematical model used in this investigation included classical static and dynamic derivatives estimated through the analysis of a variety of PID maneuvers.

Resulting time history comparisons, along with the examination of the derivative estimates, have shown that the final estimates are adequate representations of the dynamic system. The estimates of the normal force coefficients, in general, indicated clear trends, exhibited very good consistency along with a limited level of scatter, and a reasonable size for the Cramer-Rao bounds. The estimates of the pitching moment coefficients were found to be best extracted from flight data pertaining to the PPSS and PPSSTV maneuvers with their inherent ability to sustain excitation in pitch rate. Consequently, these maneuvers also produced the most consistent results for the dynamic coefficients C_{Nq} and C_{mq} in comparison with estimates obtained from other maneuvers. The normal force and moment coefficients due to pitch vane deflection were found to be best identified using the PPSSTV class maneuvers. Overall, very good agreement of the estimates with the tunnel data was obtained at lower angles of attack with some deviations apparent at higher alphas. The majority of the rolling and yawing moment coefficients, indicated good consistency with well defined trends and limited scatter present mostly at higher alphas. However, although discernible trends are still evident, less consistency in the estimates was achieved for the cross-coupling control derivatives $C_{n\delta a}$, $C_{n\delta dht}$ and $C_{l\delta r}$ than the primary control derivatives $C_{l\delta a}$, $C_{l\delta dht}$ and $C_{n\delta r}$.

References

1- Iliff, K.W., Taylor, L.W., "Determination of Stability Derivatives From Flight Data Using A Newton-Raphson Minimization Technique", NASA TN D-6579, 1972.

2- Iliff, K.W., Maine, R.E., "Practical Aspects of Using A Maximum Likelihood Estimation Method to Extract Stability and Control Derivatives From Flight Data", NASA TN D-8209, 1976.

3- Maine, Richard, E., and Murray, James, E., "pEst Version 2.1 User's Manual", NASA TM 88280, 1987.

4- Maine, Richard, E., Iliff, Kenneth, W., "Application of Parameter Estimation to Aircraft Stability and Control, The Output-Error Approach", NASA RF 1168, 1986.

5- Maine, Richard E., Iliff, Kenneth, W. "Identification of Dynamic Systems ; Theory and Formulation, NASA RP-1138, 1985.

6- Maine, Richard E., Iliff, K.W., "The Theory and Practice of Estimating the Accuracy of Dynamic Flight-Determined Coefficients", NASA RP-1077, 1981.

7- Napolitano, M. R., et. al., "Parameter Estimation for the NASA F/A-18 HARV at High Angles of Attack", AIAA paper 94-3504, Atmospheric Flight Mechanics Conference, Scottsdale, AZ, August 1994.

8- Napolitano, M. R., et. al., "Parameter Estimation for a Cessna U-206 Aircraft Using the Maximum Likelihood Method", AIAA paper 94-3481, Atmospheric Flight Mechanics Conference, Scottsdale, AZ, August 1994.

9- Paris, Alfonso, "Determination of the Stability and Control Derivatives from Flight Data for the MAE Cessna U-206", Thesis WVU MAE Dept., Morgantown, WV, May 1994.

10- Regenie, Victoria, et. al., "The F-18 High Alpha Research Vehicle: A High-Angle-of-Attack Testbed Aircraft", NASA TM-104253, 1992.

11- Roskam, Jan, Airplane Flight Dynamics and Automatic Flight Controls, Roskam Aviation and Engineering Corporation, Ottawa, Kansas, 1982.

List of Tables

Table 1: Breakdown of aerodynamic coefficients estimated for each class of maneuver analyzed.

Table 2: Listing of the elements for the diagonal weighting matrix W_1 used for each class of maneuver.

Table 3: Breakdown of aerodynamic coefficients estimated for each class of maneuver analyzed.

Table 4: Listing of the elements for the diagonal weighting matrix W_1 used for each class of maneuver.

Table 1: Breakdown of aerodynamic coefficients estimated for each class of maneuver analyzed.
(✓ = Parameter was estimated, W/T = Coefficient held constant at wind tunnel value,
N/A = Surface was not active and thus no estimate was obtained)

PARAMETER	SSI MD	OLON	3211	PPSS	PPSSTV
C_{No}	✓	✓	✓	✓	✓
$C_{N\alpha}$	✓	✓	✓	✓	✓
$C_{N\delta e}$	✓	✓	✓	✓	W/T
$C_{N\delta tef}$	✓	W/T	W/T	W/T	W/T
$C_{N\delta lef}$	W/T	W/T	W/T	W/T	W/T
$C_{N\delta pv}$	✓	✓	✓	N/A	✓
$C_{N\delta sa}$	✓	N/A	N/A	N/A	N/A
C_{Nq}	✓	✓	✓	✓	✓
C_{mo}	✓	✓	✓	✓	✓
$C_{m\alpha}$	✓	✓	✓	✓	✓
$C_{m\delta e}$	✓	✓	✓	✓	W/T
$C_{m\delta tef}$	✓	W/T	W/T	W/T	W/T
$C_{m\delta lef}$	W/T	W/T	W/T	W/T	W/T
$C_{m\delta pv}$	✓	✓	✓	N/A	✓
$C_{m\delta sa}$	✓	N/A	N/A	N/A	N/A
C_{mq}	✓	✓	✓	✓	✓
C_{Ao}	✓	✓	✓	✓	✓
$C_{A\alpha}$	✓	✓	✓	✓	✓
$C_{A\delta e}$	✓	✓	✓	✓	W/T
$C_{A\delta tef}$	✓	W/T	W/T	W/T	W/T
$C_{A\delta lef}$	W/T	W/T	W/T	W/T	W/T
$C_{A\delta pv}$	✓	✓	✓	N/A	✓
$C_{A\delta sa}$	✓	N/A	N/A	N/A	N/A
C_{Aq}	✓	✓	✓	✓	✓
a_{nBias}	✓	✓	✓	✓	✓
a_{xBias}	✓	✓	✓	✓	✓

Table 2: Listing of the elements for the diagonal weighting matrix W_1 used for each class of maneuver.

MANEUVER	A	B	C	D	E
SSI MD	3	8	5	150	140*
OLON	3	8	5	150	140
3211	3	8	5	50	40
PPSS	5	8	4	150	250
PPSSTV	3	8	5	150	140

* For the SSI MD maneuver at an alpha of 60° E=250

Table 3: Breakdown of aerodynamic coefficients estimated for each class of maneuver analyzed. (✓ = Parameter was estimated, W/T = Coefficient held constant at wind tunnel value, N/A = Surface was not active and thus no estimate was obtained)

PARAMETER	SSI MD	OLAT	PYRS	PYRSTV
C_{Yo}	✓	✓	✓	✓
$C_{Y\beta}$	✓	✓	✓	✓
$C_{Y\delta a}$	✓	✓	W/T*	✓
$C_{Y\delta dht}$	✓	N/A	W/T	W/T
$C_{Y\delta r}$	✓	✓	✓	W/T
$C_{Y\delta yv}$	✓	N/A	N/A	✓
C_{Yp}	✓	✓	✓	✓
C_{Yr}	✓	✓	✓	✓
C_{lo}	✓	✓	✓	✓
$C_{l\beta}$	✓	✓	✓	✓
$C_{l\delta a}$	✓	✓	✓	✓
$C_{l\delta dht}$	✓	N/A	W/T	W/T
$C_{l\delta r}$	✓	✓	W/T*	W/T
$C_{l\delta yv}$	✓	N/A	N/A	✓
C_{lp}	✓	✓	✓	✓
C_{lr}	✓	✓	✓	✓
C_{no}	✓	✓	✓	✓
$C_{n\beta}$	✓	✓	✓	✓
$C_{n\delta a}$	✓	✓	W/T	✓
$C_{n\delta dht}$	✓	N/A	W/T	W/T
$C_{n\delta r}$	✓	✓	✓	W/T
$C_{n\delta yv}$	✓	N/A	N/A	✓
C_{np}	✓	✓	✓	✓
C_{nr}	✓	✓	✓	✓
a_{yBias}	✓	✓	✓	✓

* Indicates parameter was estimated for all alpha higher than 20°

Table 4: Listing of the elements for the diagonal weighting matrix W_1 used for each class of maneuver.

MANEUVER	A	B	C	D	E
SSI MD	12	3*	17	3*	200
OLAT	12	6	17	6	200
PYRS	12	3	17	3	200
PYRSTV	12	3*	17	3*	200

* For the SSI MD and PYRSTV maneuvers at an alpha of 60° B=6, D=6

List of Figure Captions

Figure 1 - Block diagram of the parameter identification process

Figure 2 - Sample time histories showing representative a) SSI MD OBES inputs, b) OLON elevator OBES inputs, c) 3211 elevator OBES inputs, d) PPSS elevator pilot input and e) PPSSTV elevator pilot input

Figure 3 - Sample time history indicating clear correlations between a) angle of attack, leading-edge flap and trailing-edge flap deflection and b) elevator and pitch vane deflection

Figure 4 - Measured (——) and computed (-------) SSI MD time history comparison plots for $\alpha = 30°$

Figure 5 - PID results for $C_{N\_b\alpha}$, $C_{m\_b\alpha}$, $C_{N\delta e}$ and $C_{m\delta e}$ with Cramer-Rao bounds for $\alpha = 5° - 60°$ in comparison with wind tunnel data points and estimate curve fit

Figure 6 - PID results for $C_{N\delta\alpha}$, $C_{m\delta\alpha}$, $C_{N\delta tef}$ and $C_{m\delta tef}$ with Cramer-Rao bounds for $\alpha = 20° - 60°$ in comparison with wind tunnel data points and estimate curve fit

Figure 7 - PID results for $C_{N\delta pv}$, $C_{m\delta pv}$, C_{Nq} and C_{mq} with Cramer-Rao bounds for $\alpha = 5° - 60°$ including an estimate curve fit generated using PPSS and PPSSTV estimates exclusively

Figure 8 - Comparison in pitch rate response generated by a) SSI MD, b) PPSS and c) PPSSTV inputs for $\alpha = 20°$

Figure 9 - Sample time histories showing representative a) SSI MD OBES control inputs, (b) OLAT OBES control inputs, (c) PYRS Pilot control inputs and (d) PYRSTV Pilot control inputs

Figure 10 - Sample time history showing clear correlations between aileron, differential horizontal tail and rudder deflections for the PYRS maneuver

Figure 11 - Sample time history showing clear correlations between aileron, differential horizontal tail, rudder and yaw vane deflections for the PYRSTV maneuver

Figure 12 - Measured (——) and computed (-------) SSI MD time history comparison plots for $\alpha = 30°$

Figure 13 - PID results for $C_{l\beta}$, $C_{n\beta}$, $C_{l\delta a}$ and $C_{n\delta a}$ with Cramer-Rao bounds for $\alpha = 5° - 60°$ in comparison with wind tunnel data and estimate curve fit

Figure 14 - PID results for $C_{l\delta dht}$, $C_{n\delta dht}$, $C_{l\delta r}$ and $C_{n\delta r}$ with Cramer-Rao bounds for $\alpha = 5° - 60°$ in comparison with wind tunnel data and estimate curve fit

Figure 15 - PID results for C_{lp}, C_{nr}, C_{lr} and C_{np} with Cramer-Rao bounds for $\alpha = 5° - 60°$ in comparison with wind tunnel data and estimate curve fit

Figure 16 - PID results for $C_{y\beta}$, $C_{y\delta r}$, $C_{n\delta yv}$ and $C_{y\delta yv}$ with Cramer-Rao bounds for $\alpha = 5° - 60°$ in comparison with wind tunnel data and estimate curve fit

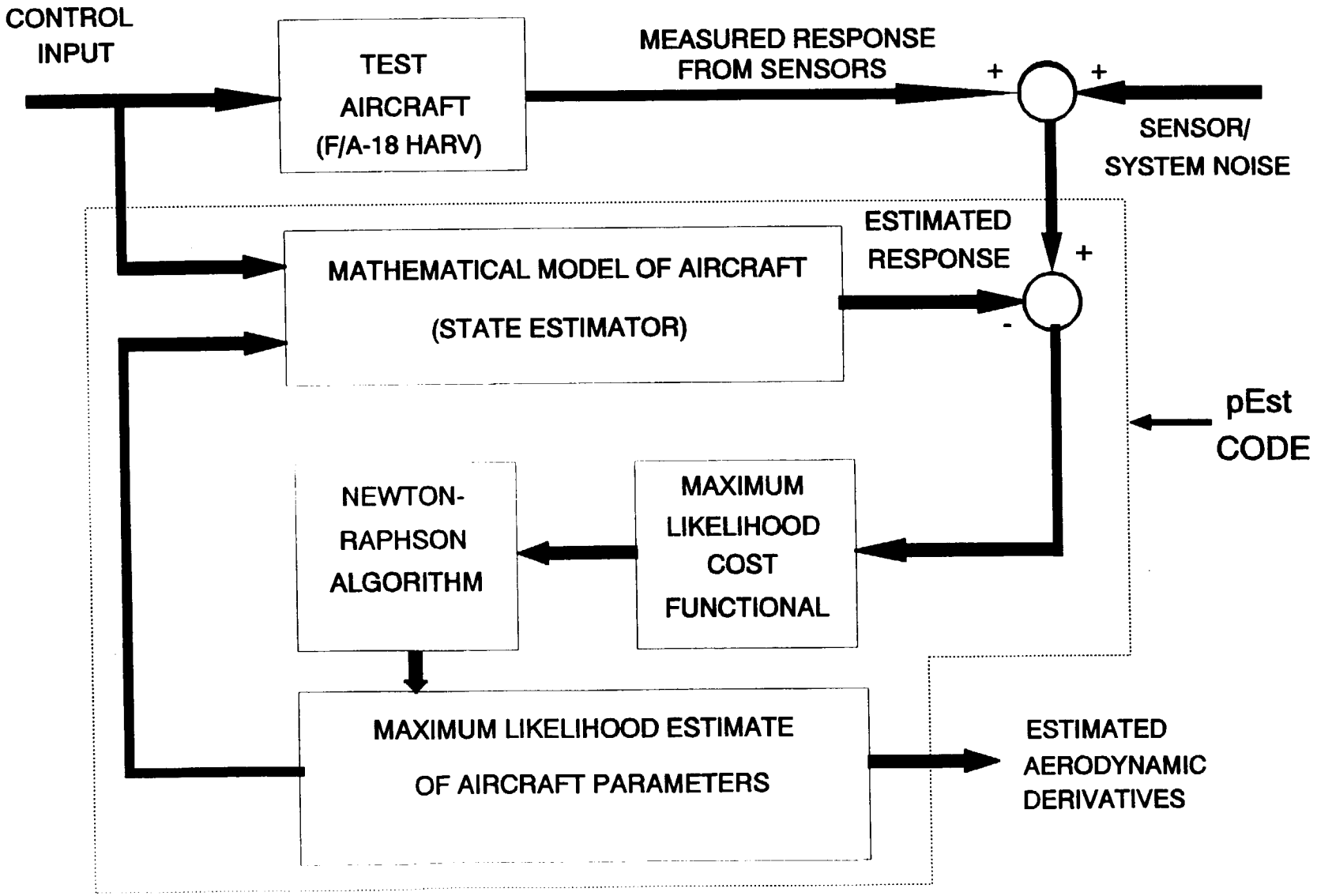
CONTROL INPUT
TEST AIRCRAFT (F/A-18 HARV)
MEASURED RESPONSE FROM SENSORS
+
+
SENSOR/ SYSTEM NOISE
ESTIMATED RESPONSE
+
-
MATHEMATICAL MODEL OF AIRCRAFT (STATE ESTIMATOR)
pEst CODE
NEWTON-RAPHSON ALGORITHM
MAXIMUM LIKELIHOOD COST FUNCTIONAL
MAXIMUM LIKELIHOOD ESTIMATE OF AIRCRAFT PARAMETERS
ESTIMATED AERODYNAMIC DERIVATIVES

(a) OBES SSI MD control inputs for alpha = 20

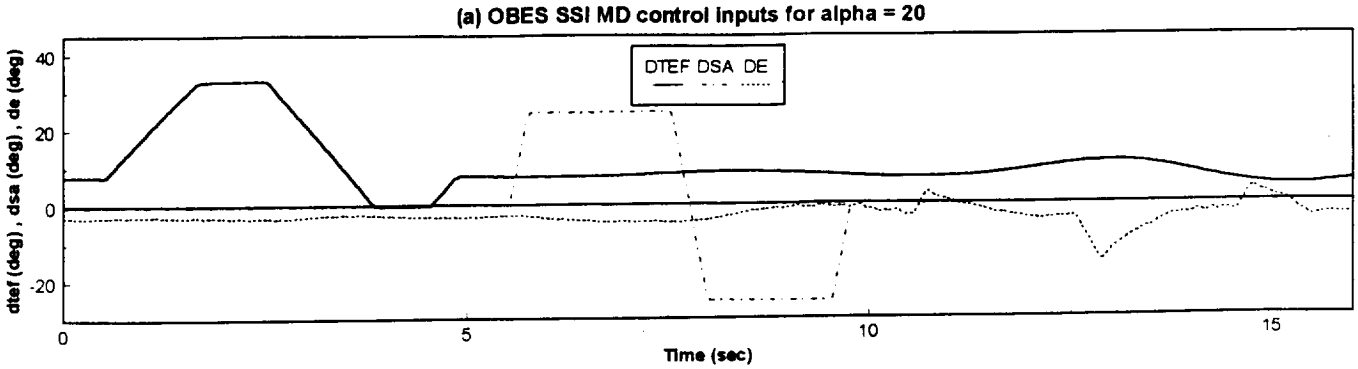

(b) OBES OLON elevator input for alpha = 20

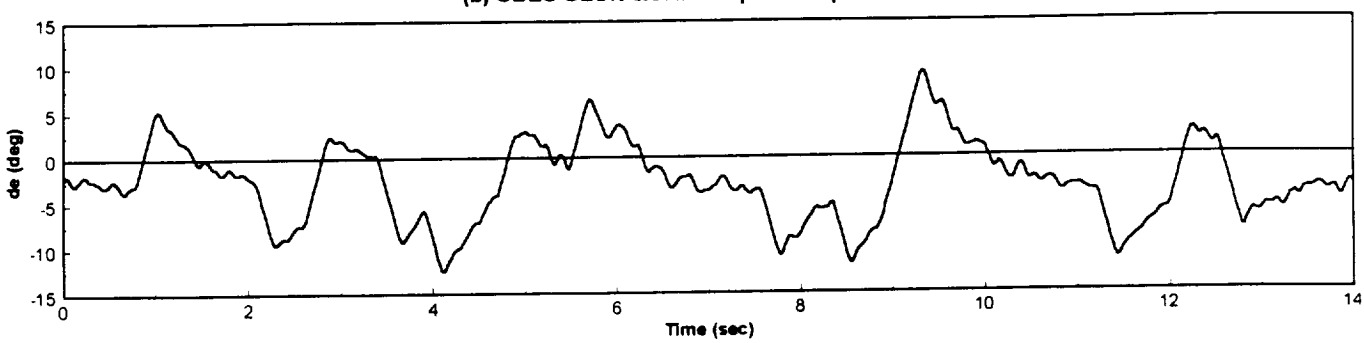

(c) OBES 3211 elevator input for alpha = 20

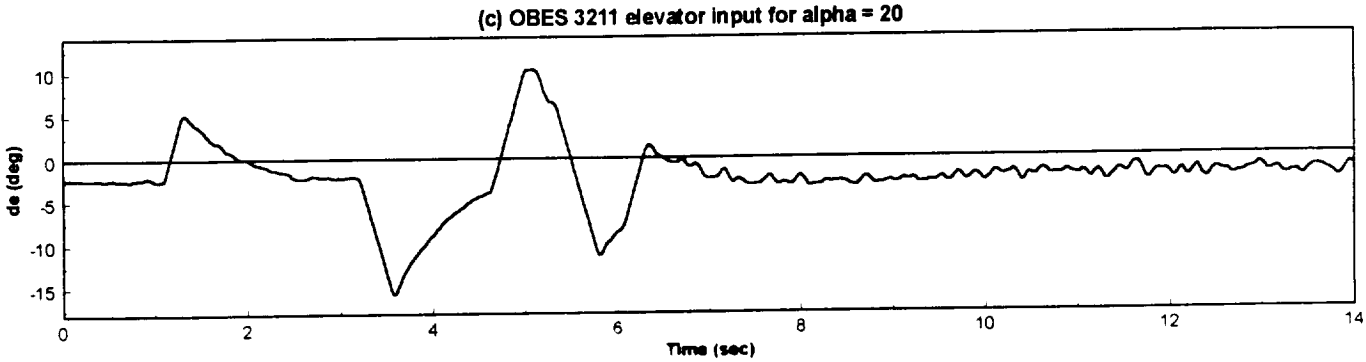

(d) PPSS Pilot elevator input for alpha = 20

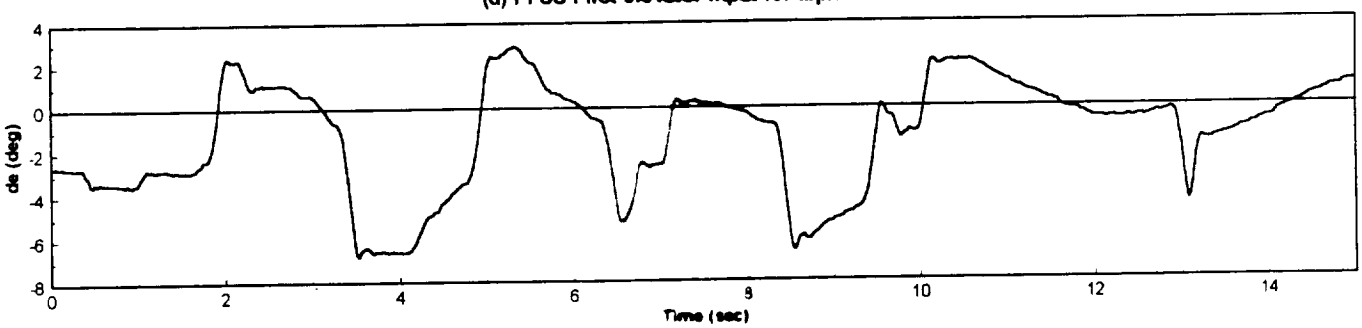

(e) PPSSTV Pilot elevator input for alpha = 20

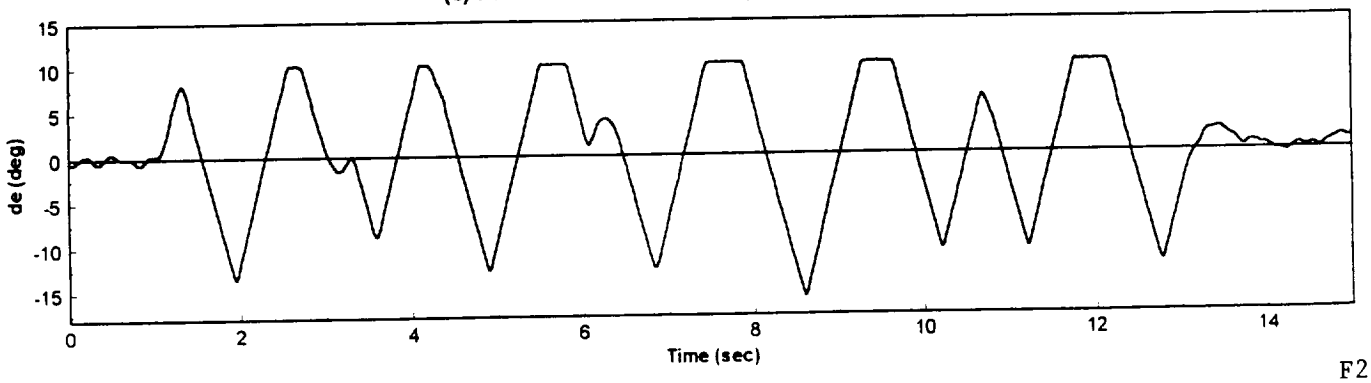

(a) General Correlation between alpha, dtef and dlef

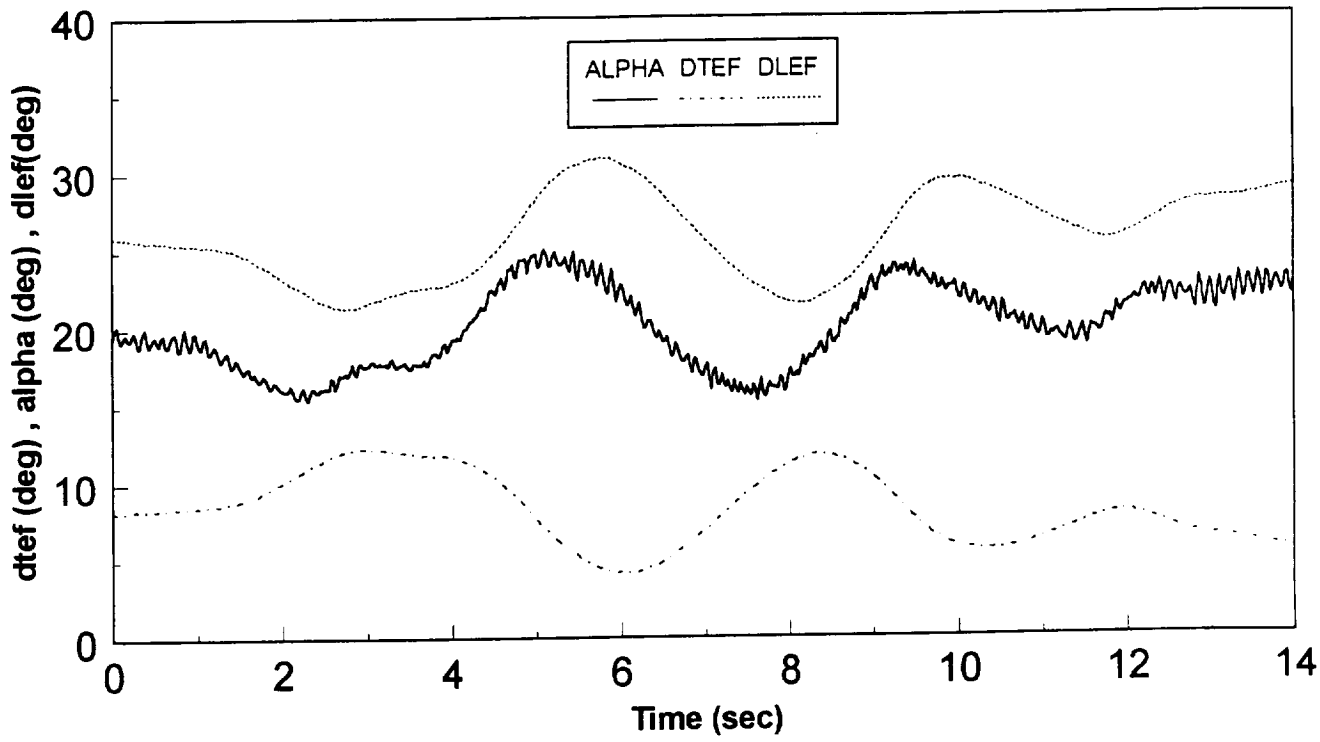

(b) Correlation between de and dpv for the PPSSTV maneuver

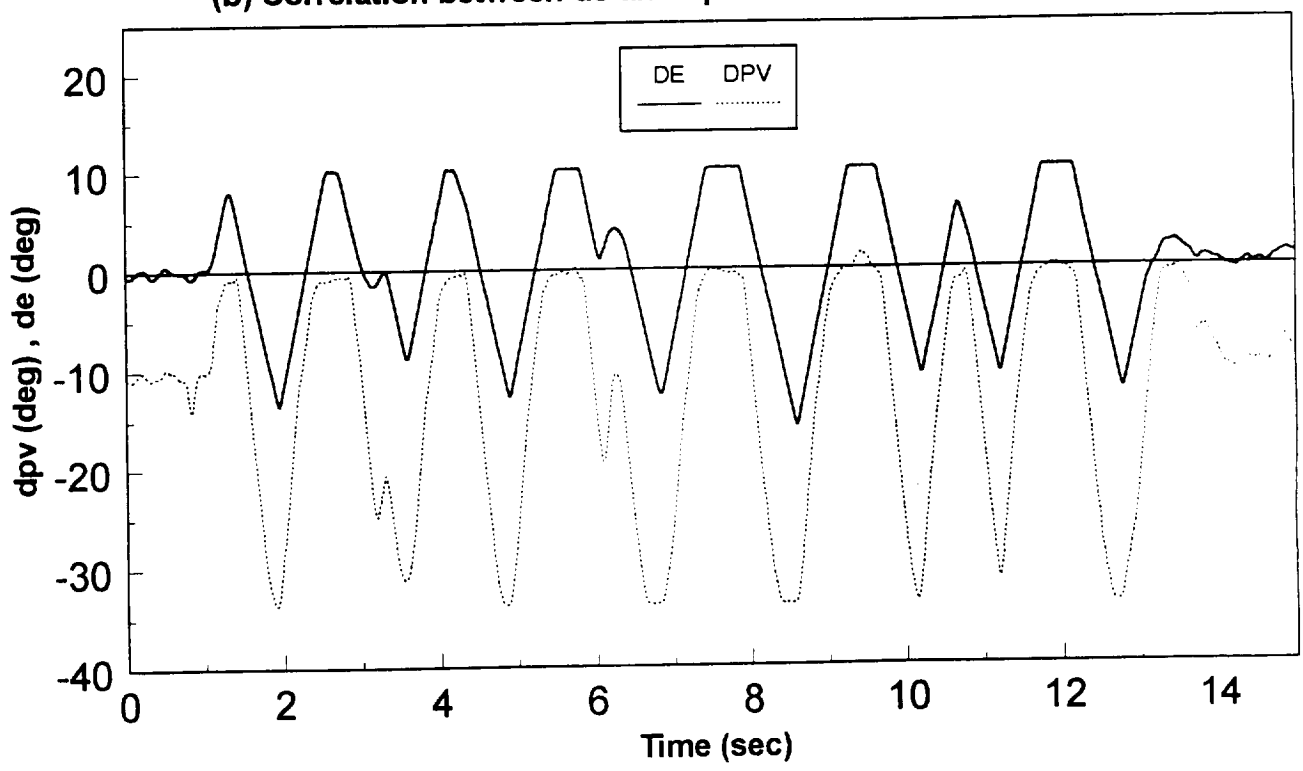

Measured and computed time histories for alpha =30

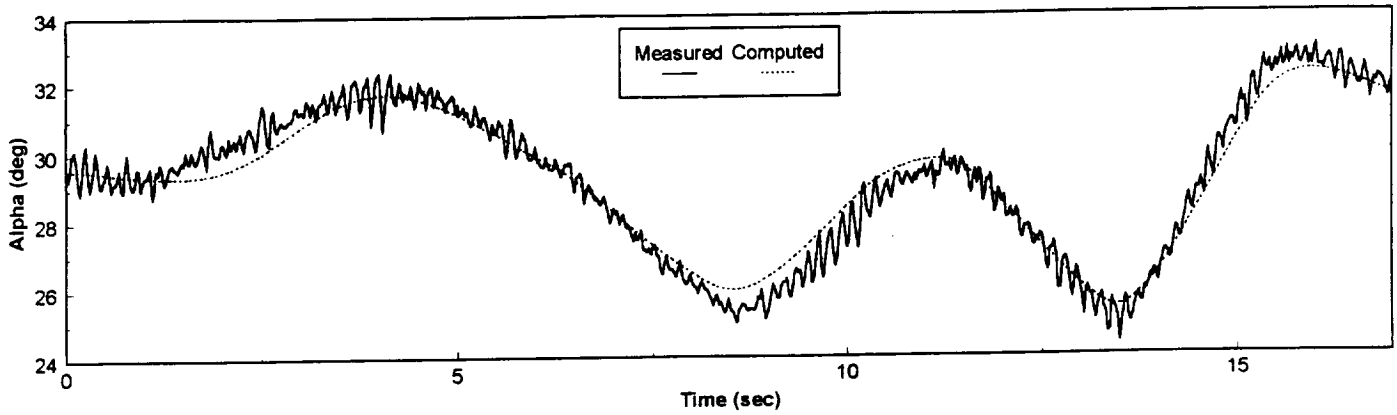

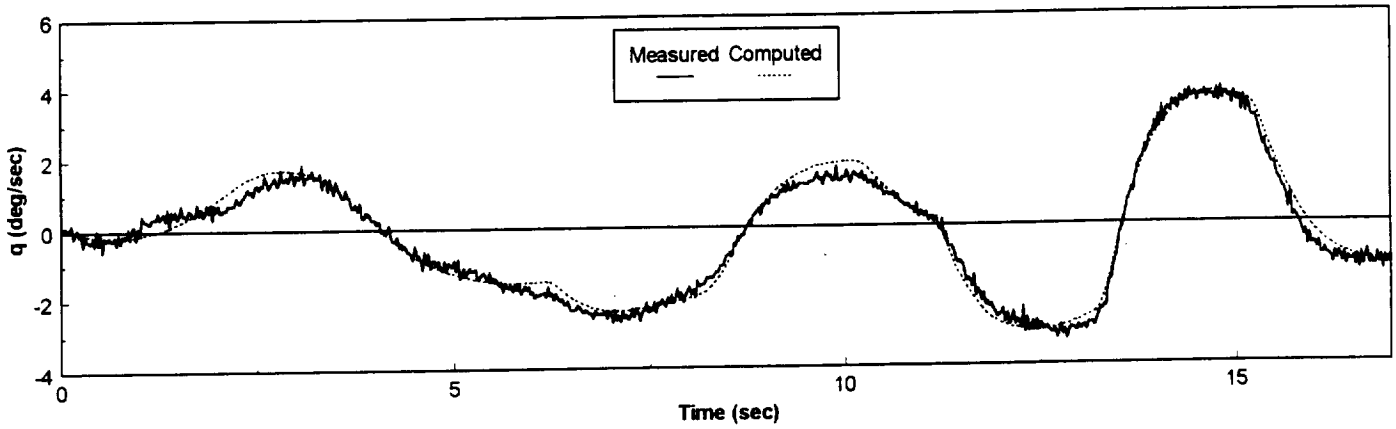

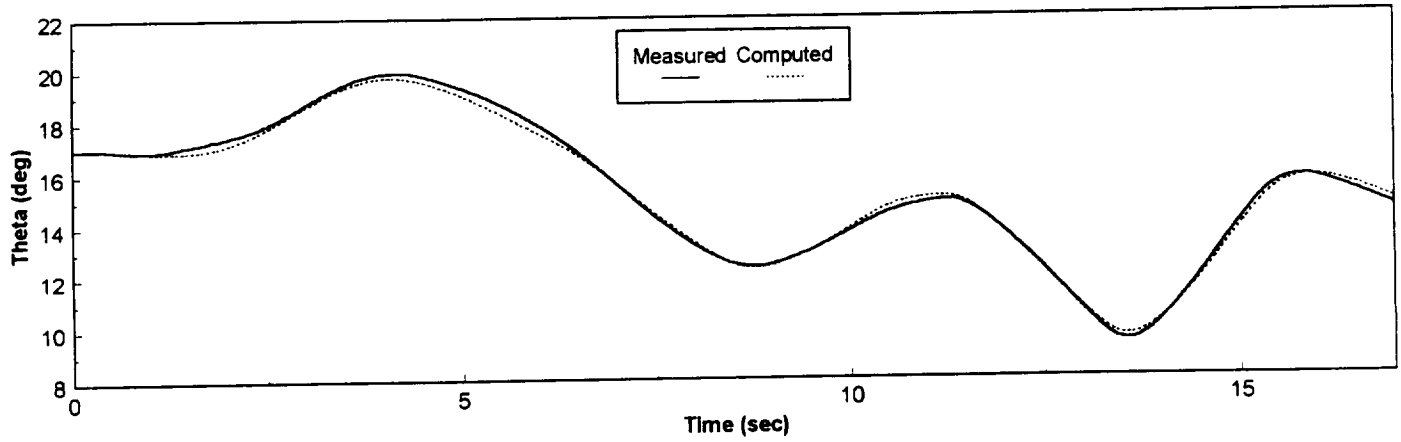

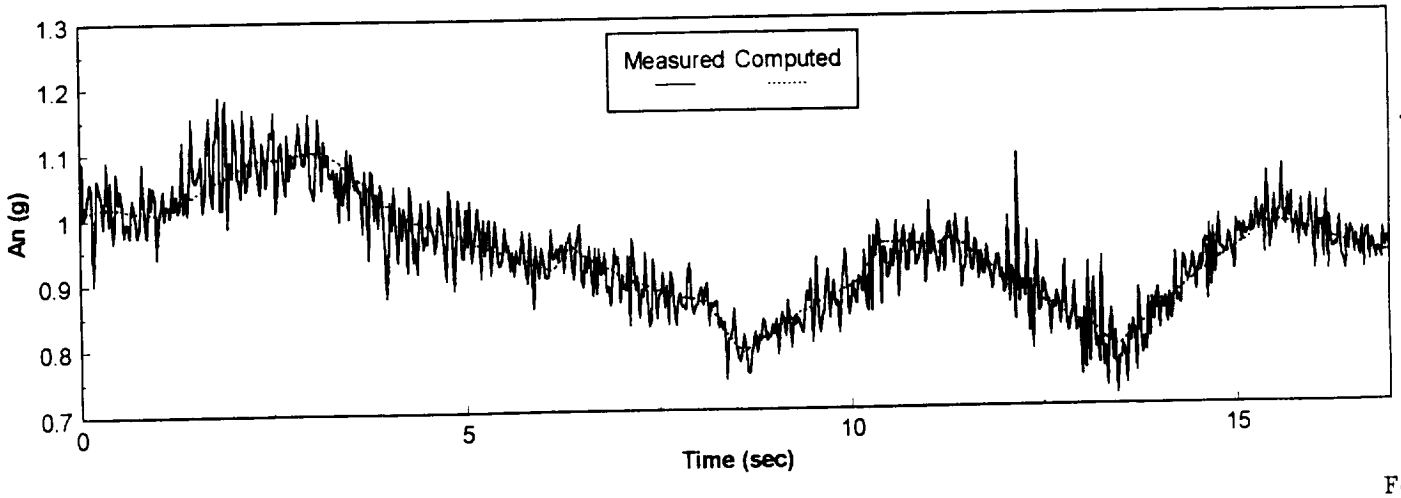

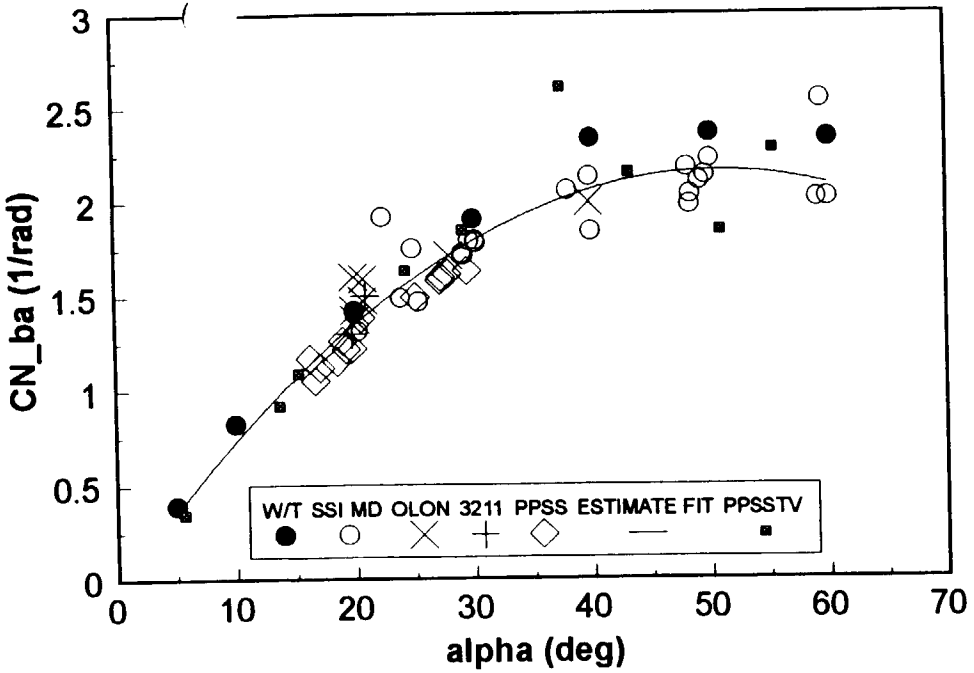
CN_ba (1/rad)
alpha (deg)
W/T SSI MD OLON 3211 PPSS ESTIMATE FIT PPSSTV

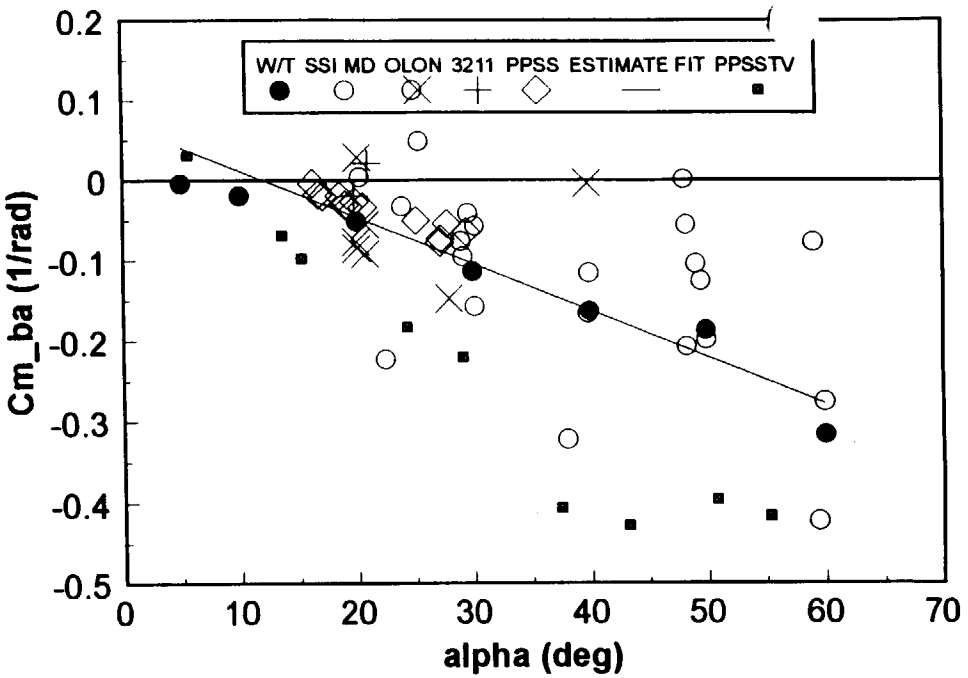
Cm_ba (1/rad)
alpha (deg)
W/T SSI MD OLON 3211 PPSS ESTIMATE FIT PPSSTV

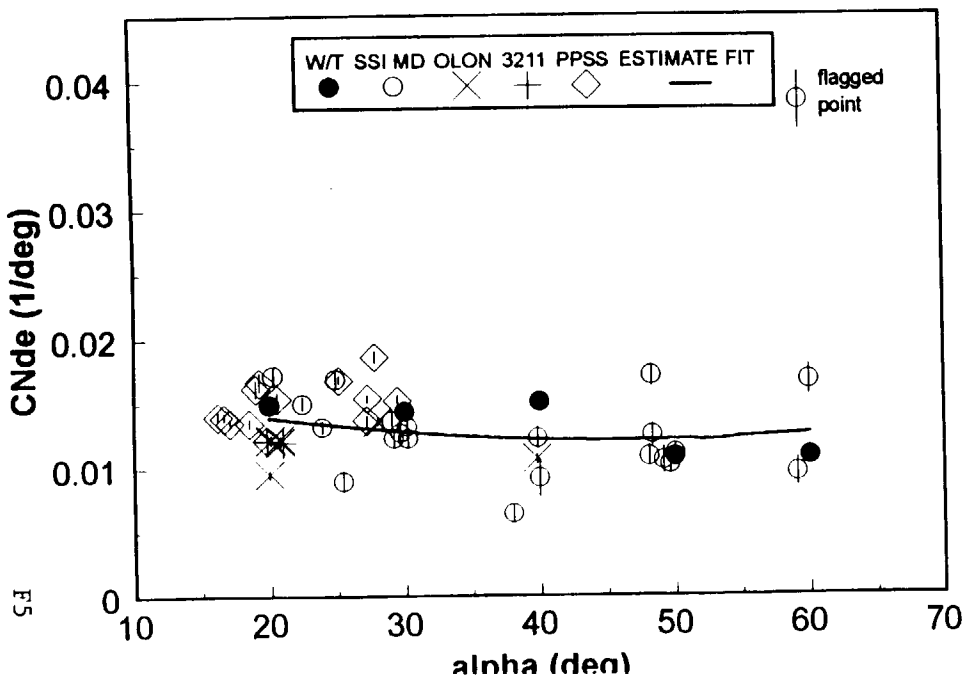
CNde (1/deg)
alpha (deg)
W/T SSI MD OLON 3211 PPSS ESTIMATE FIT
flagged point

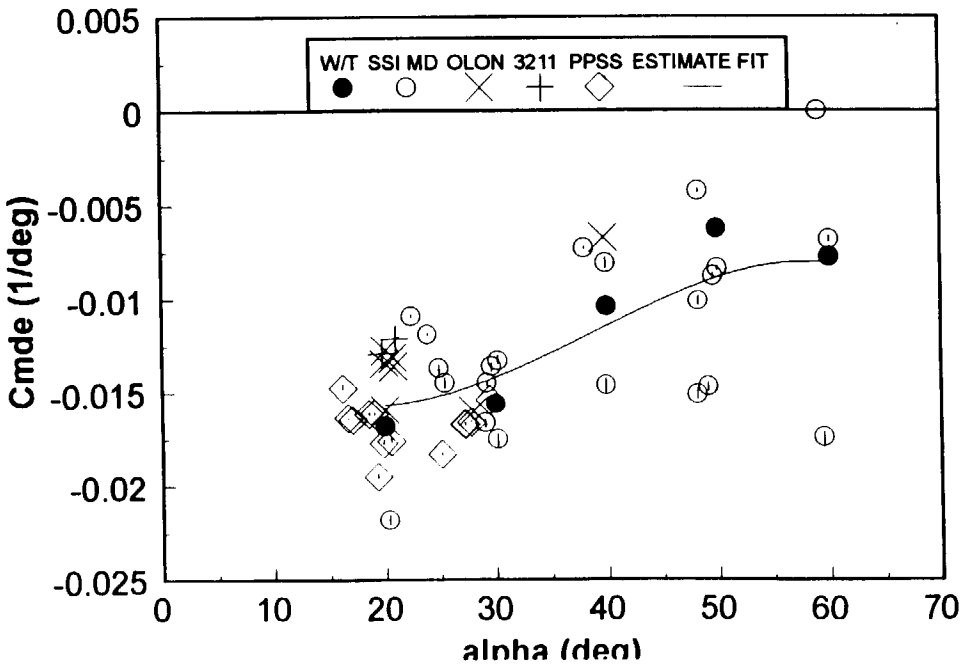
Cmde (1/deg)
alpha (deg)
W/T SSI MD OLON 3211 PPSS ESTIMATE FIT

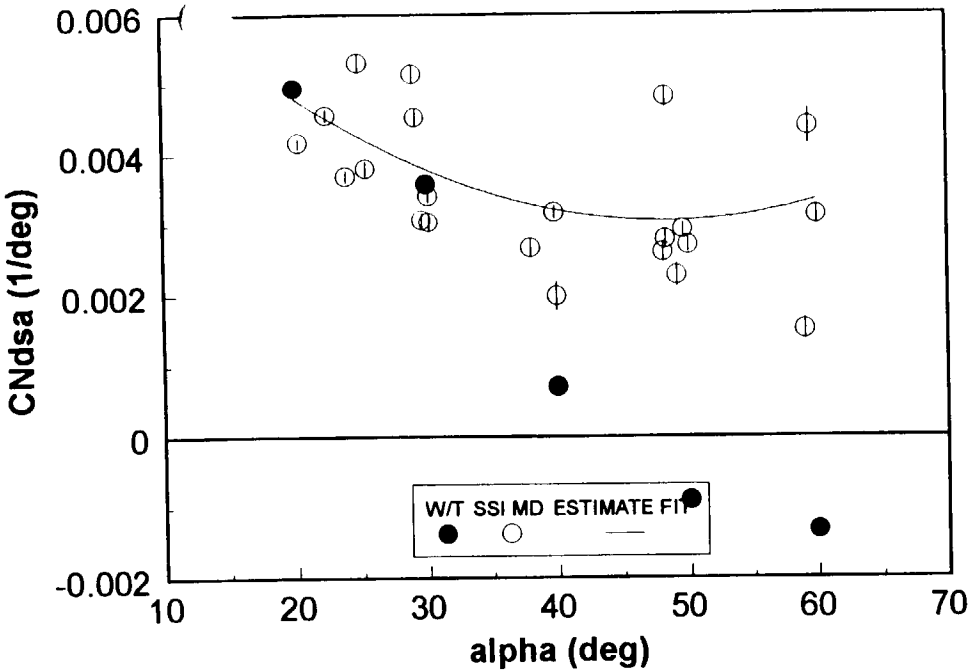
0.006
0.004
0.002
0
-0.002
CNdsa (1/deg)
10
20
30
40
50
60
70
alpha (deg)
W/T SSI MD ESTIMATE FIT

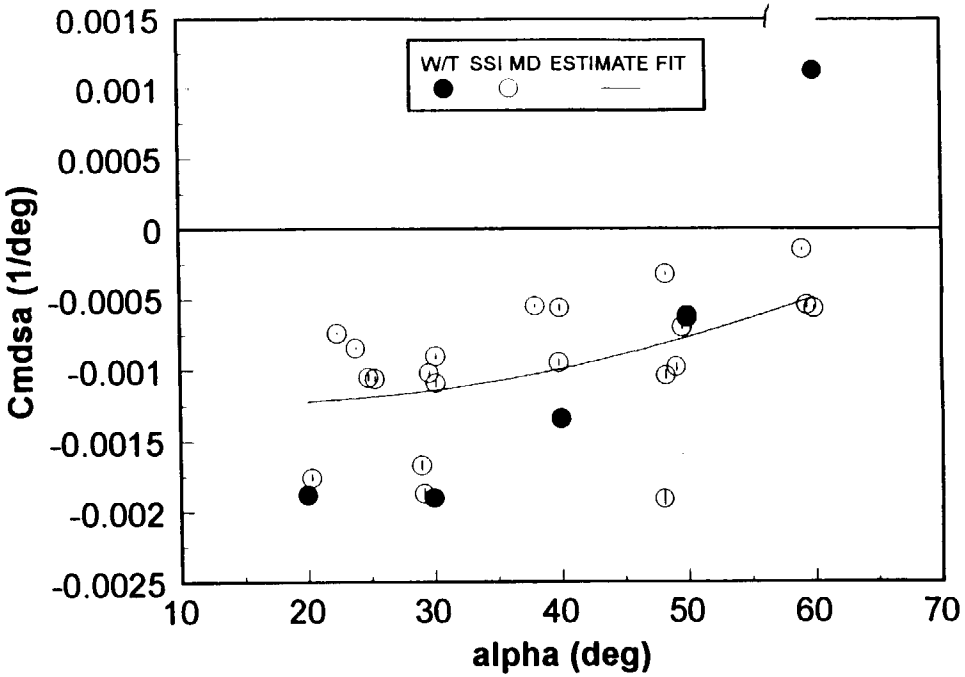
0.0015
0.001
0.0005
0
-0.0005
-0.001
-0.0015
-0.002
-0.0025
Cmdsa (1/deg)
10
20
30
40
50
60
70
alpha (deg)
W/T SSI MD ESTIMATE FIT

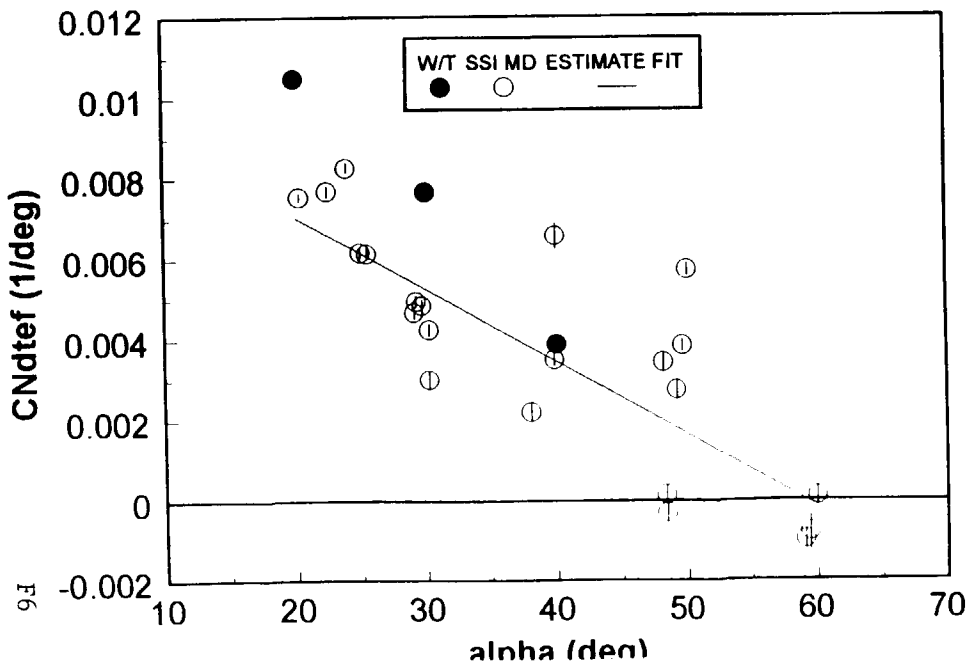
0.012
0.01
0.008
0.006
0.004
0.002
0
-0.002
CNdtef (1/deg)
10
20
30
40
50
60
70
alpha (deg)
W/T SSI MD ESTIMATE FIT

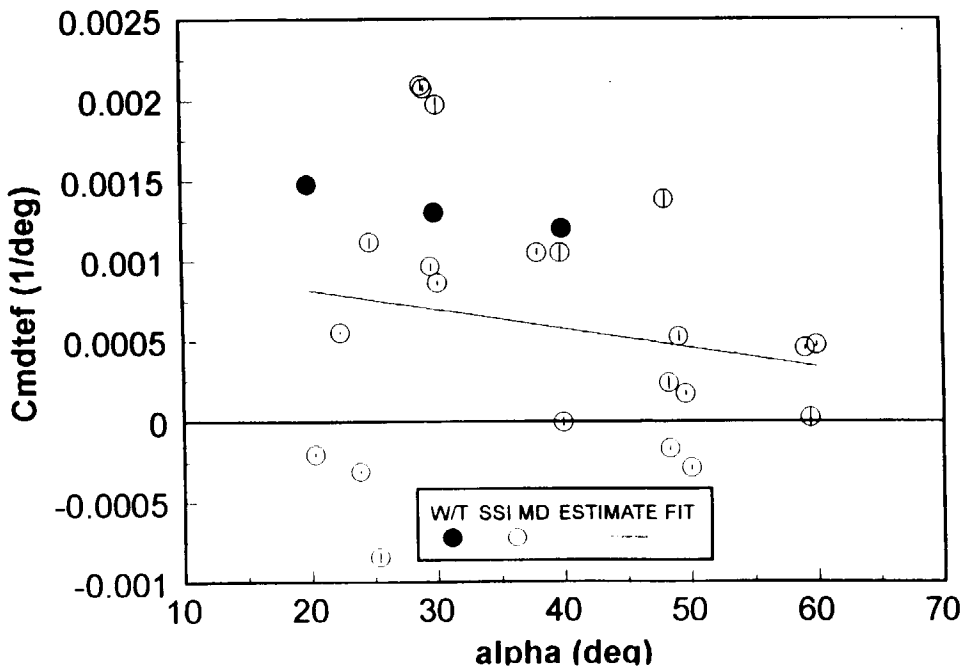
0.0025
0.002
0.0015
0.001
0.0005
0
-0.0005
-0.001
Cmdtef (1/deg)
10
20
30
40
50
60
70
alpha (deg)
W/T SSI MD ESTIMATE FIT

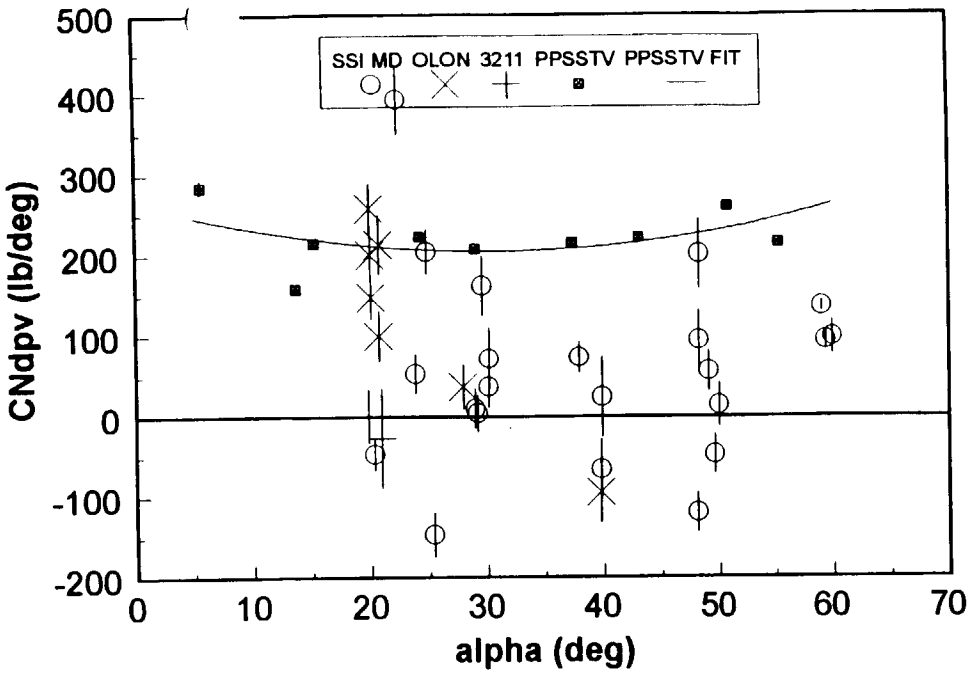
SSI MD OLON 3211 PPSSTV PPSSTV FIT
CNdpv (lb/deg)
alpha (deg)

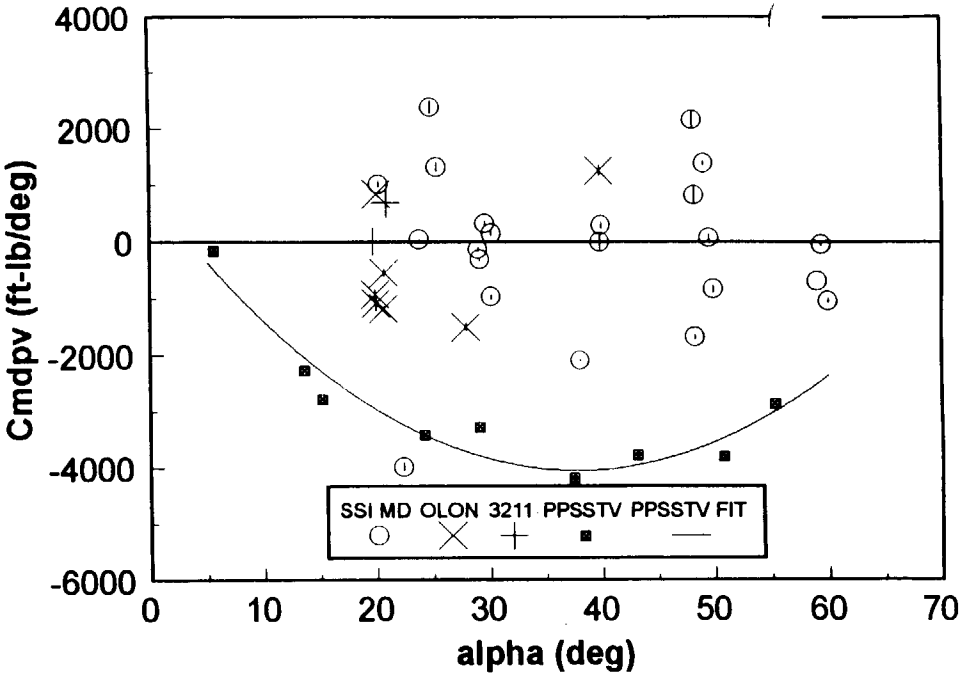
SSI MD OLON 3211 PPSSTV PPSSTV FIT
Cmdpv (ft-lb/deg)
alpha (deg)

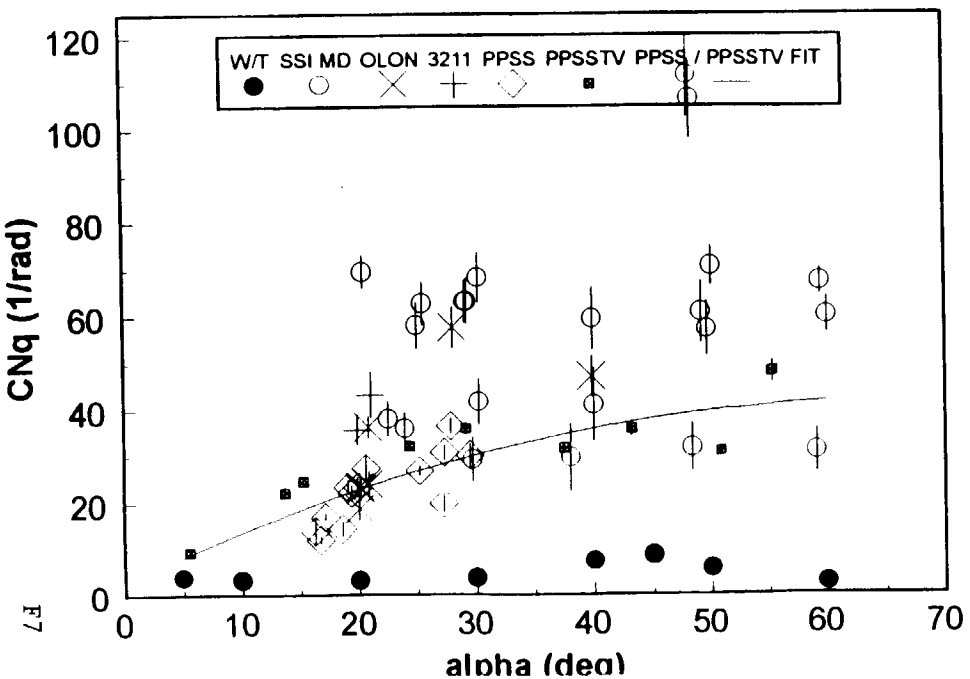
W/T SSI MD OLON 3211 PPSS PPSSTV PPSS / PPSSTV FIT
CNq (1/rad)
alpha (deg)

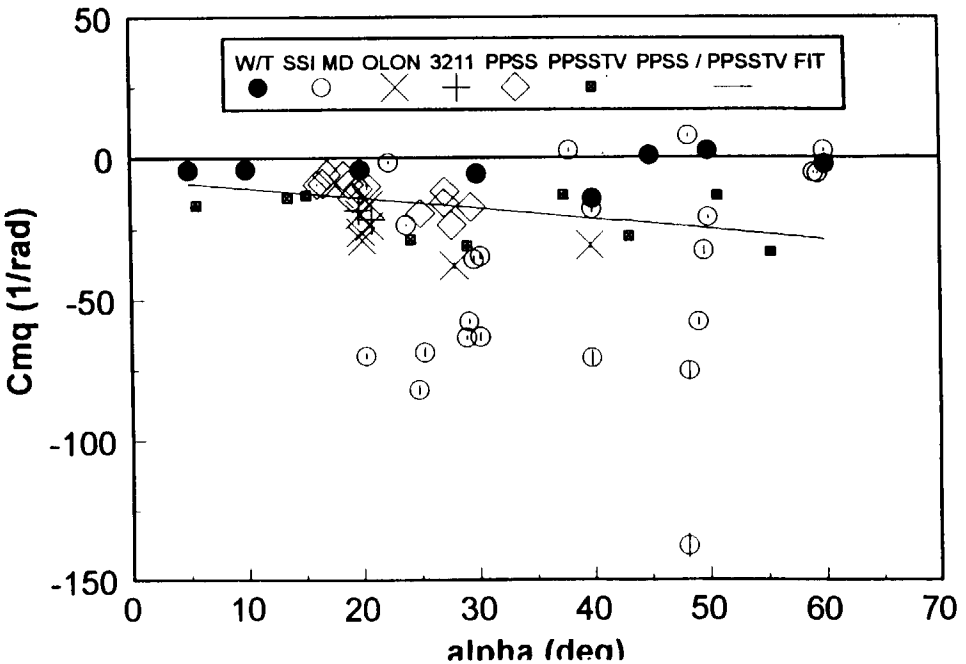
W/T SSI MD OLON 3211 PPSS PPSSTV PPSS / PPSSTV FIT
Cmq (1/rad)
alpha (deg)

(a) SSI MD pitch rate excitation

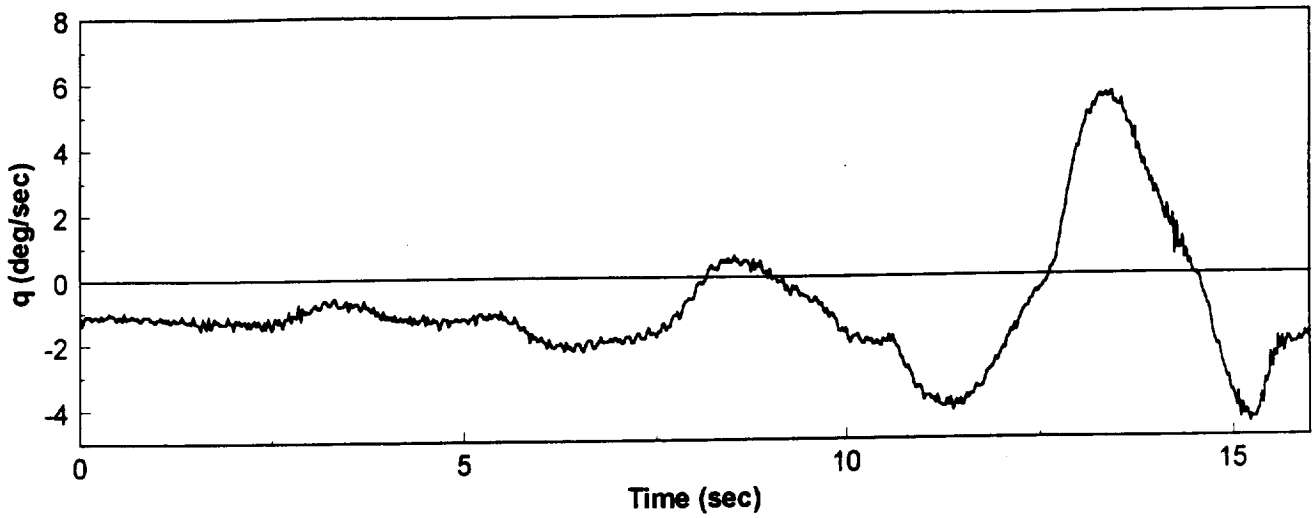

(b) PPSS pitch rate excitation

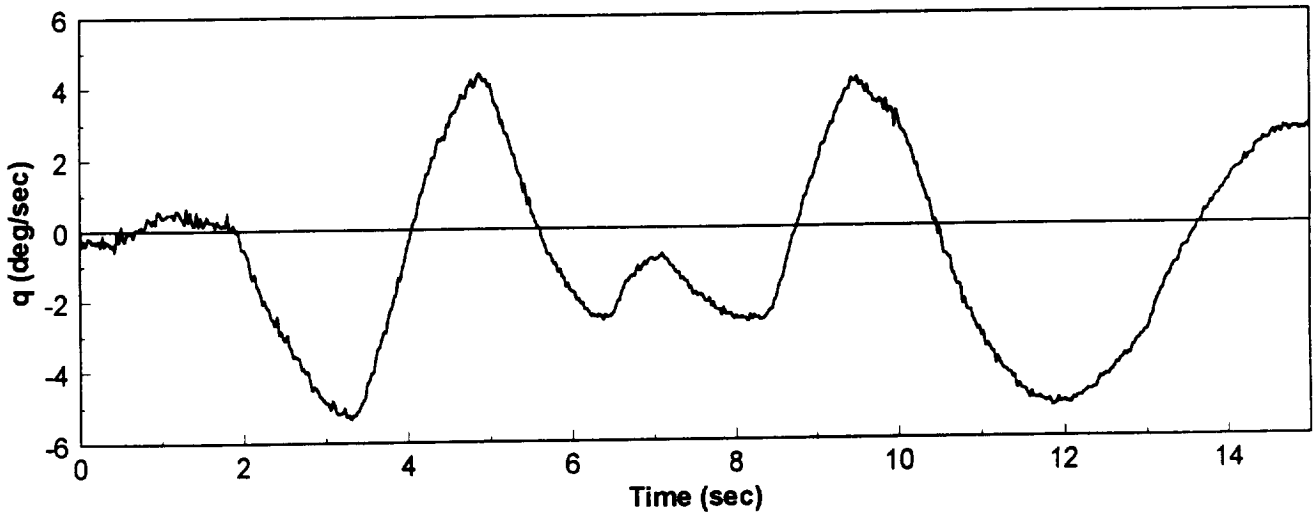

(c) PPSSTV pitch rate excitation

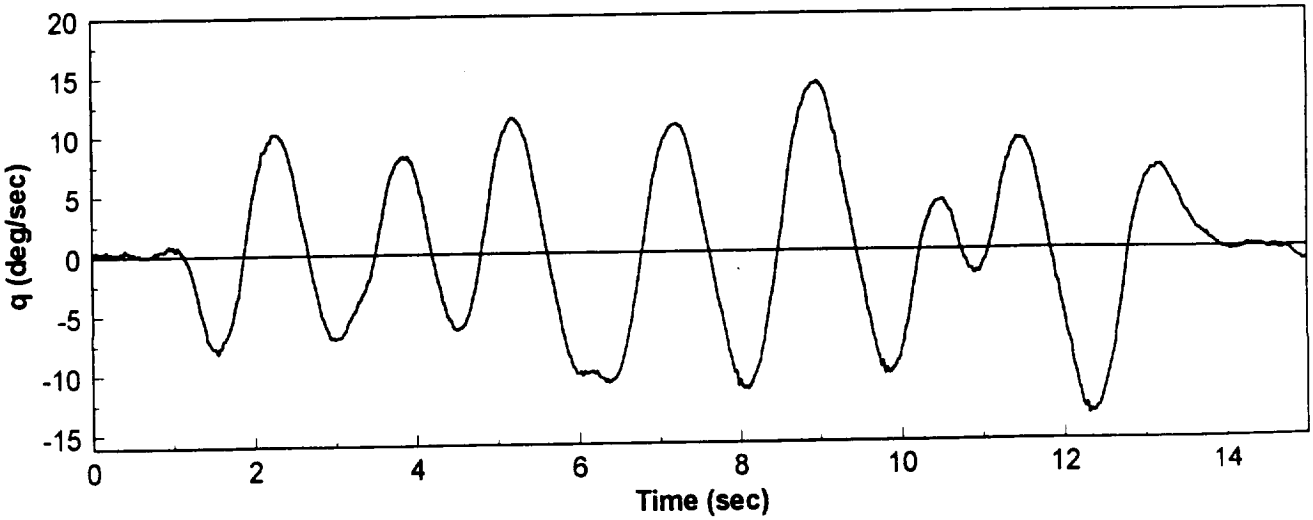

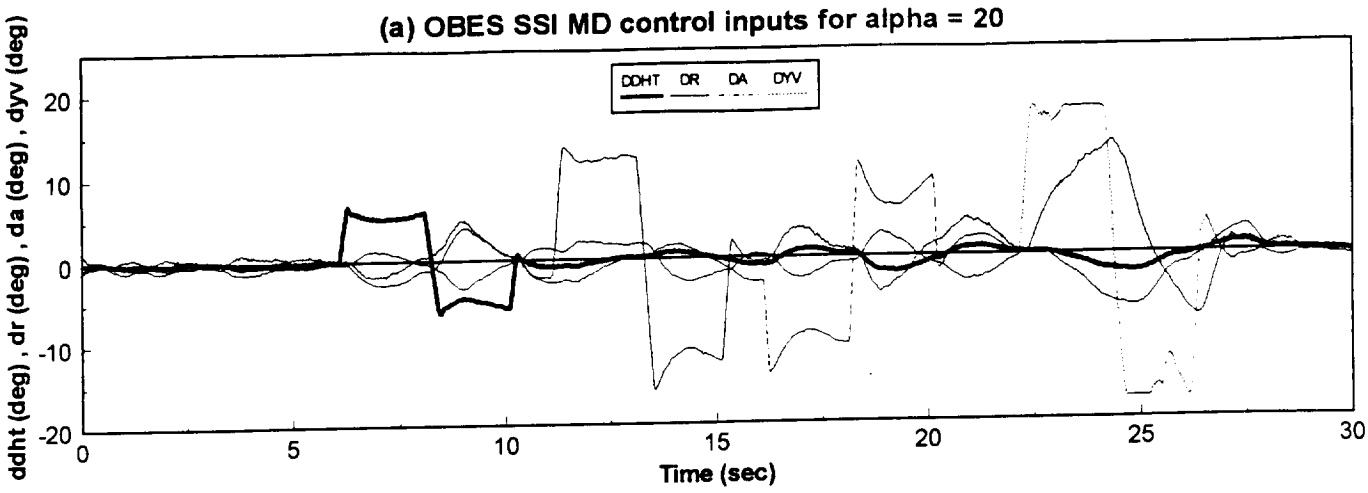
(a) OBES SSI MD control inputs for alpha = 20
DDHT DR DA DYV
ddht (deg) , dr (deg) , da (deg) , dyv (deg)
Time (sec)

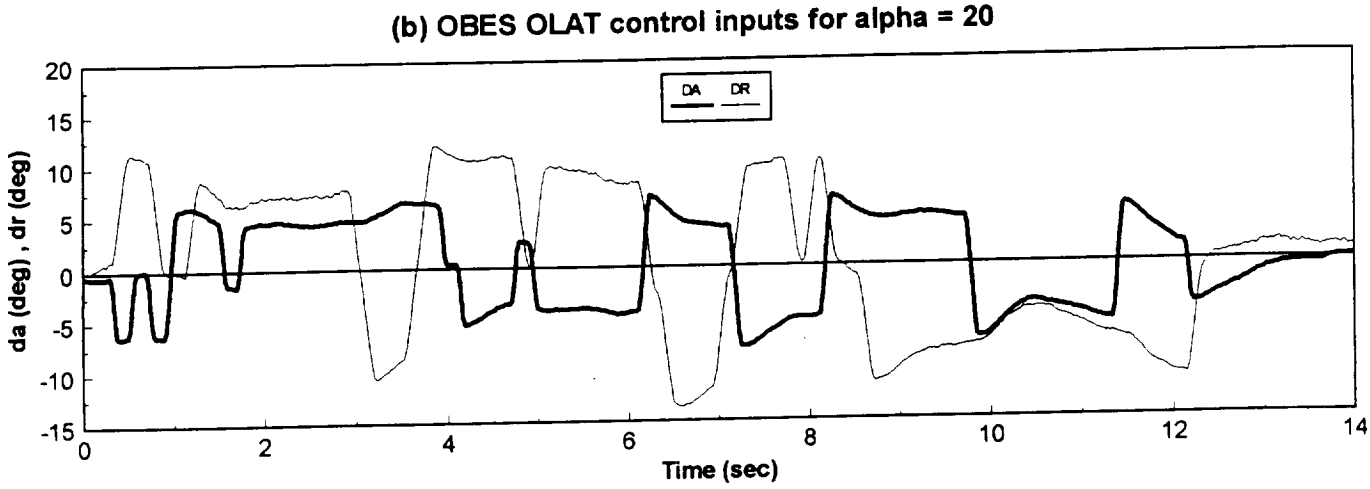
(b) OBES OLAT control inputs for alpha = 20
DA DR
da (deg) , dr (deg)
Time (sec)

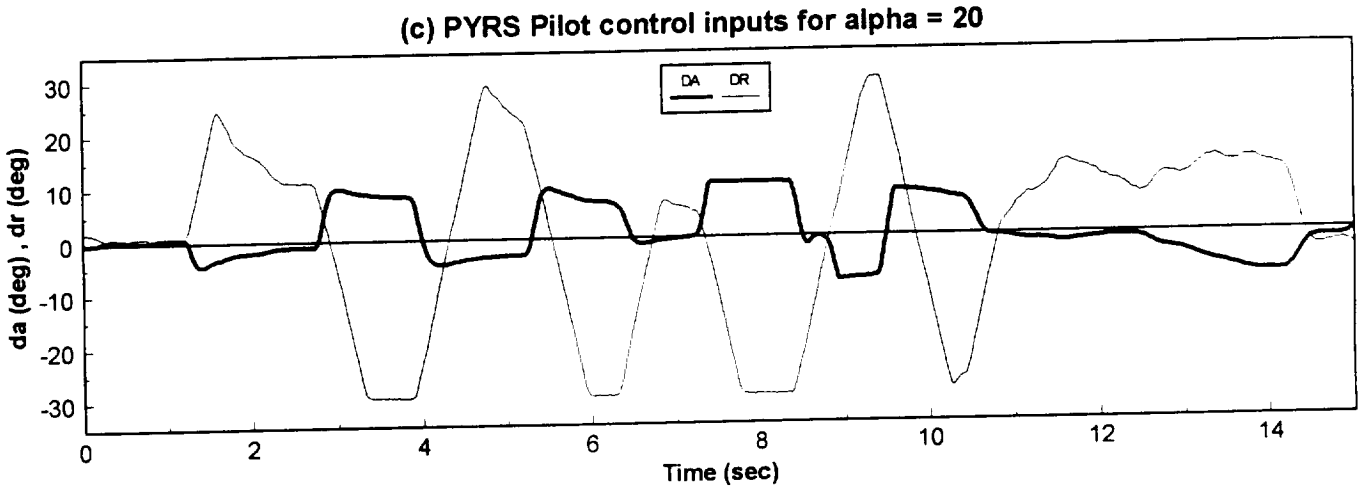
(c) PYRS Pilot control inputs for alpha = 20
DA DR
da (deg) , dr (deg)
Time (sec)

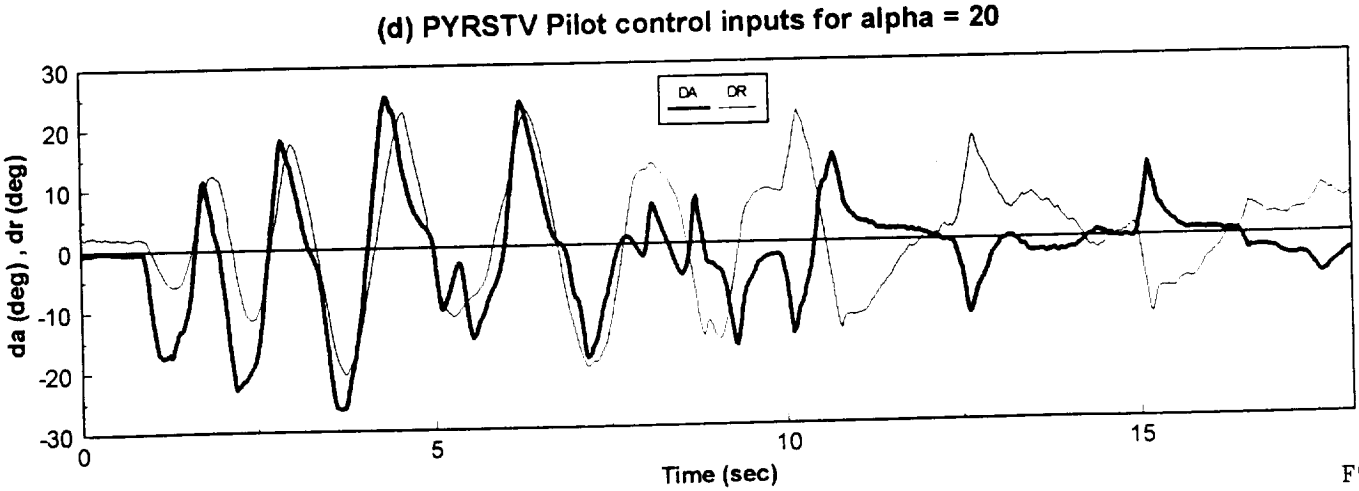
(d) PYRSTV Pilot control inputs for alpha = 20
DA DR
da (deg) , dr (deg)
Time (sec)

Correlation between da, ddht and dr for the PYRS maneuver

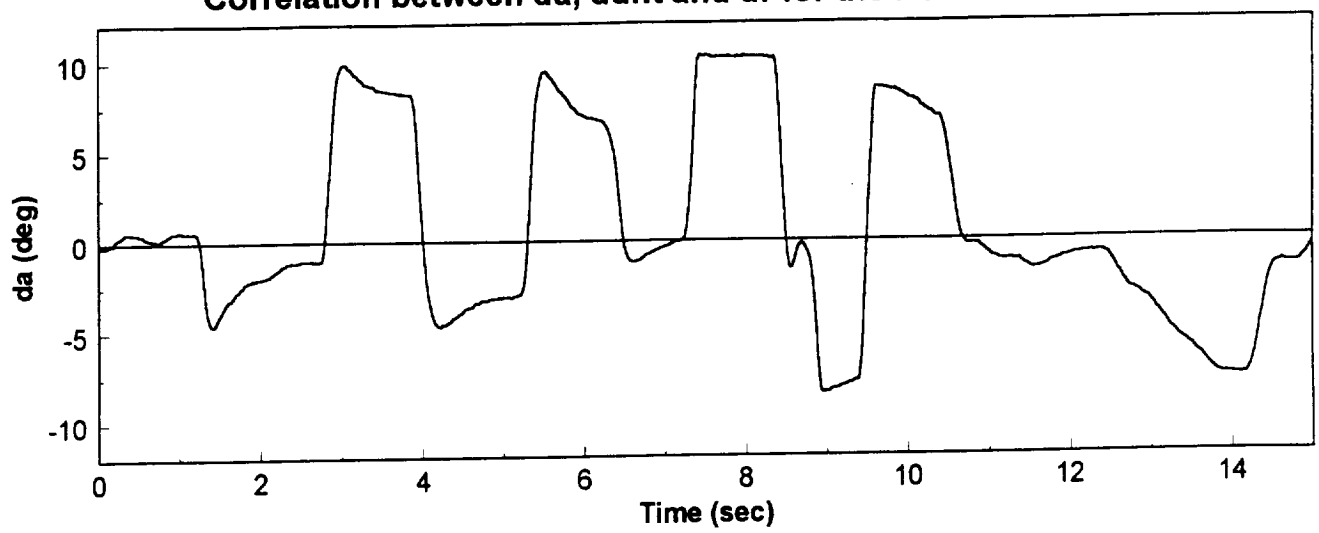

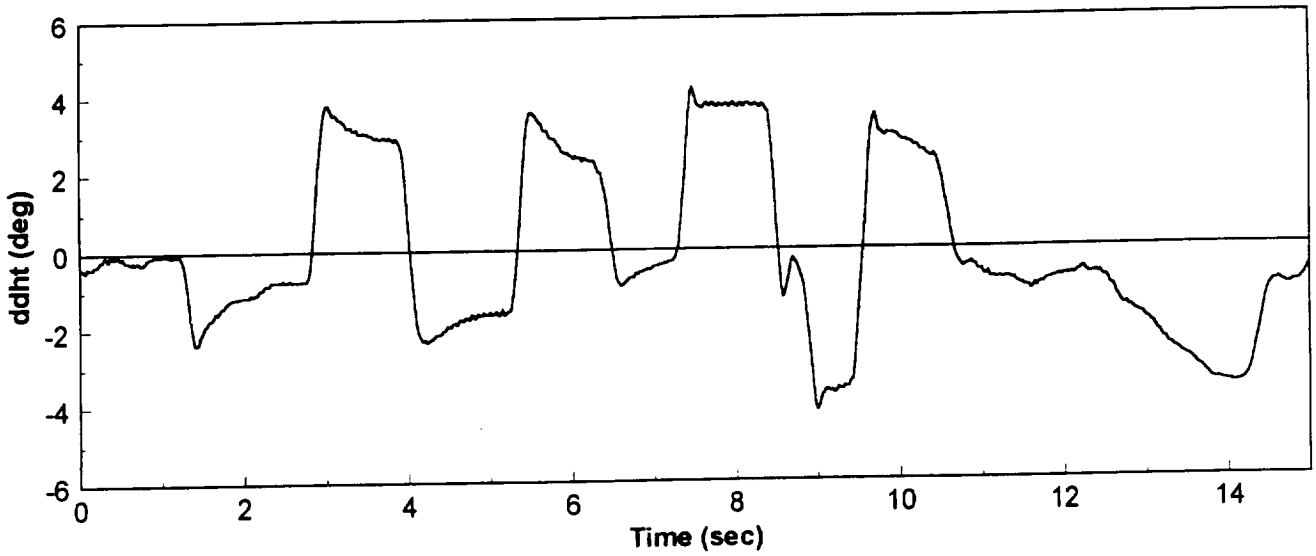

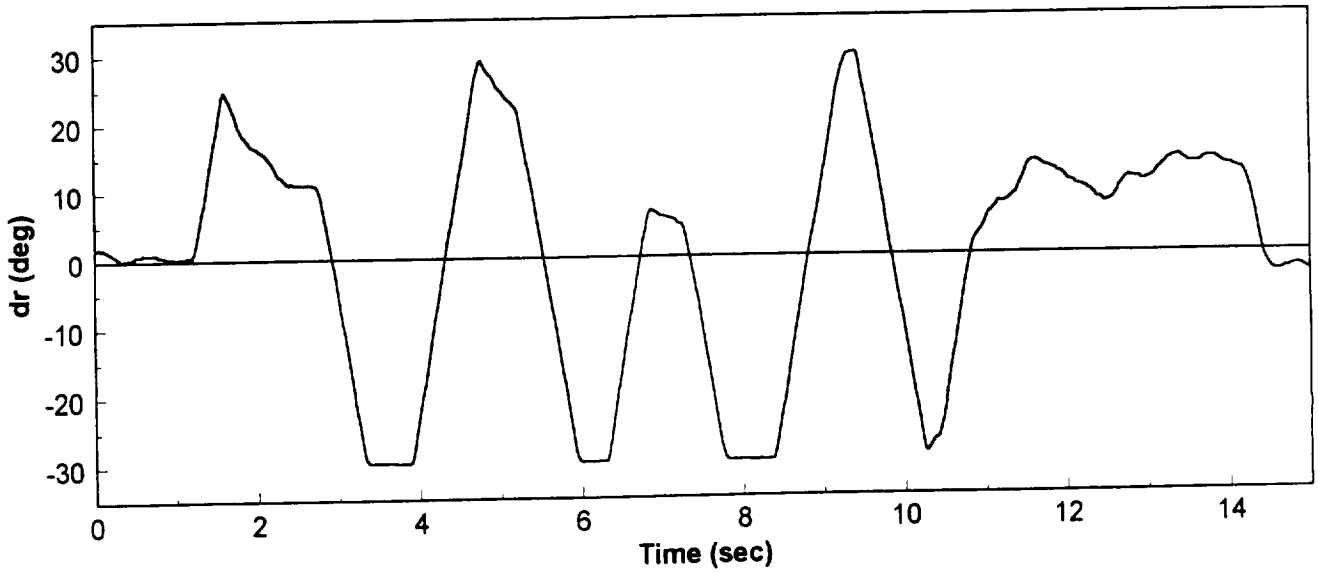

Correlation between da, ddht, dr and dyv for the PYRSTV maneuver

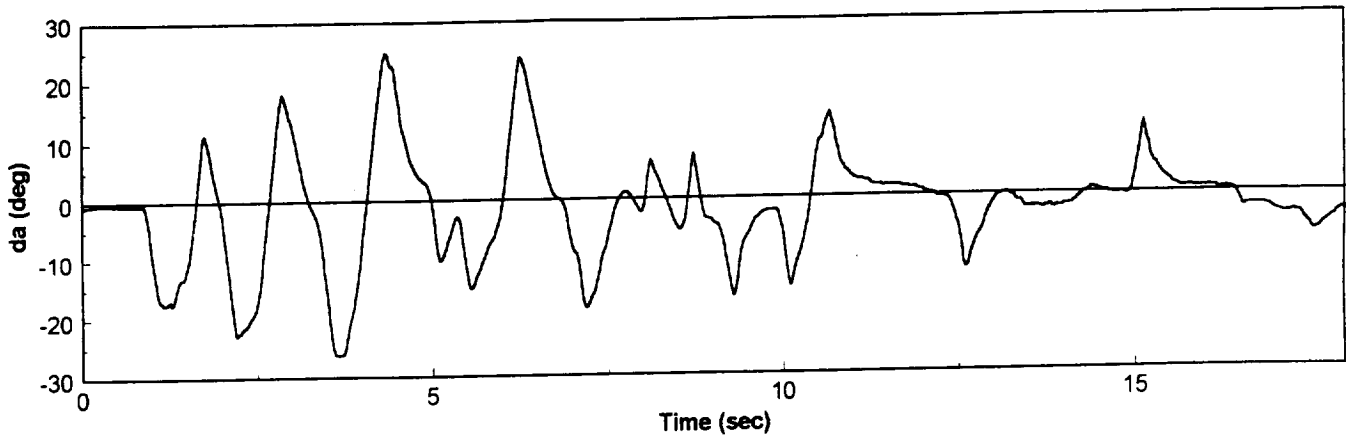

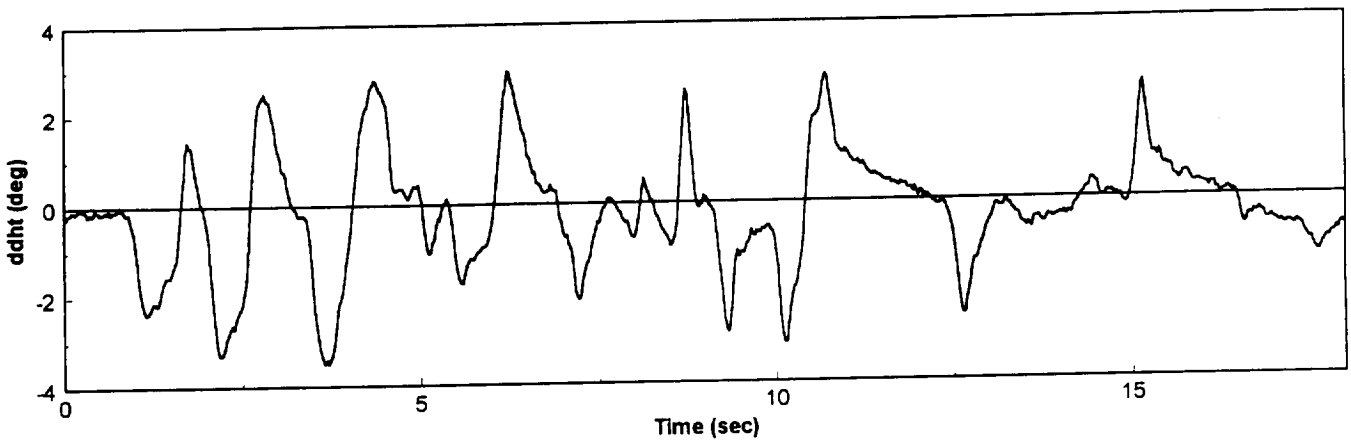

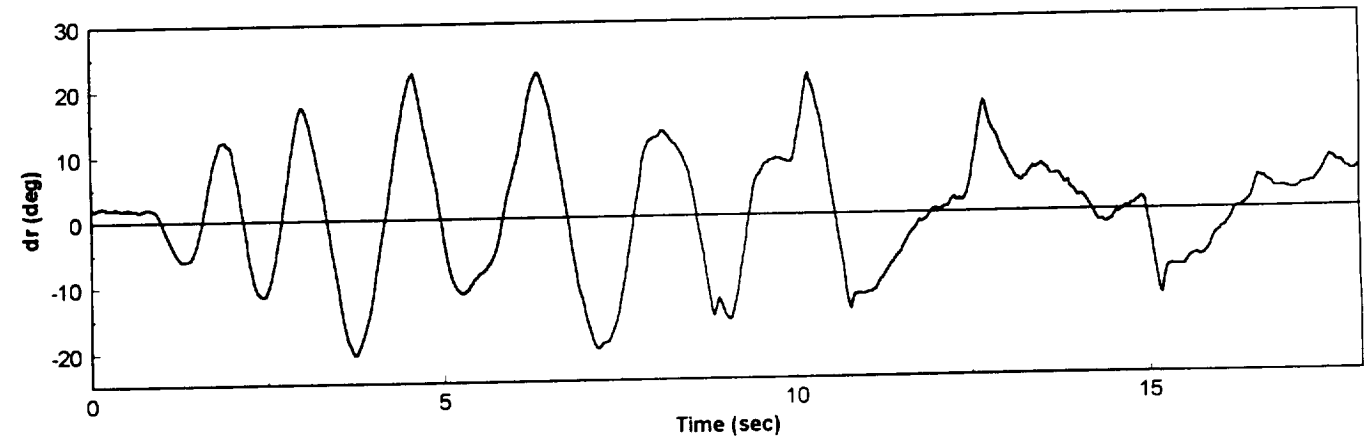

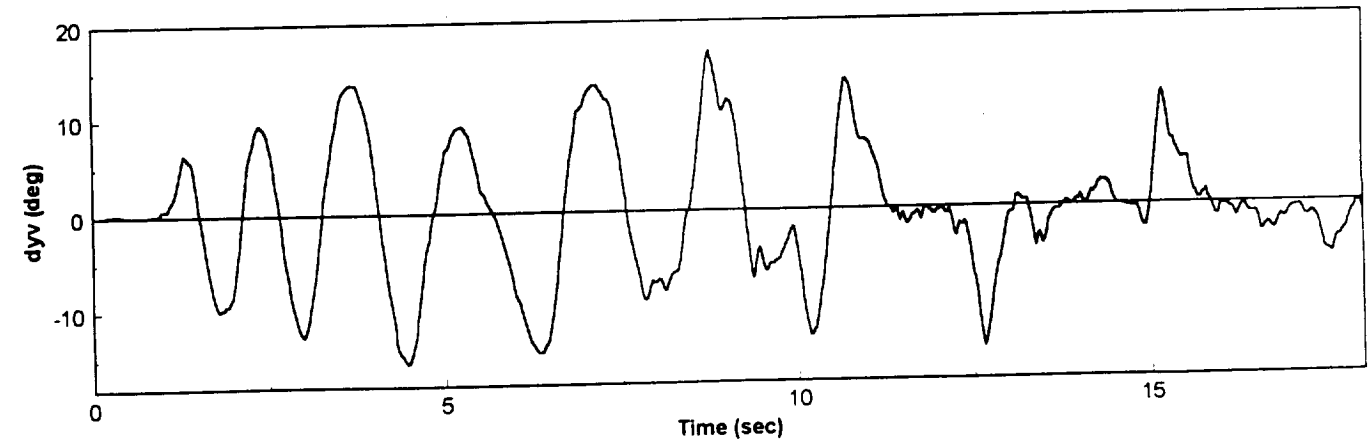

Measured and computed time histories for alpha =30

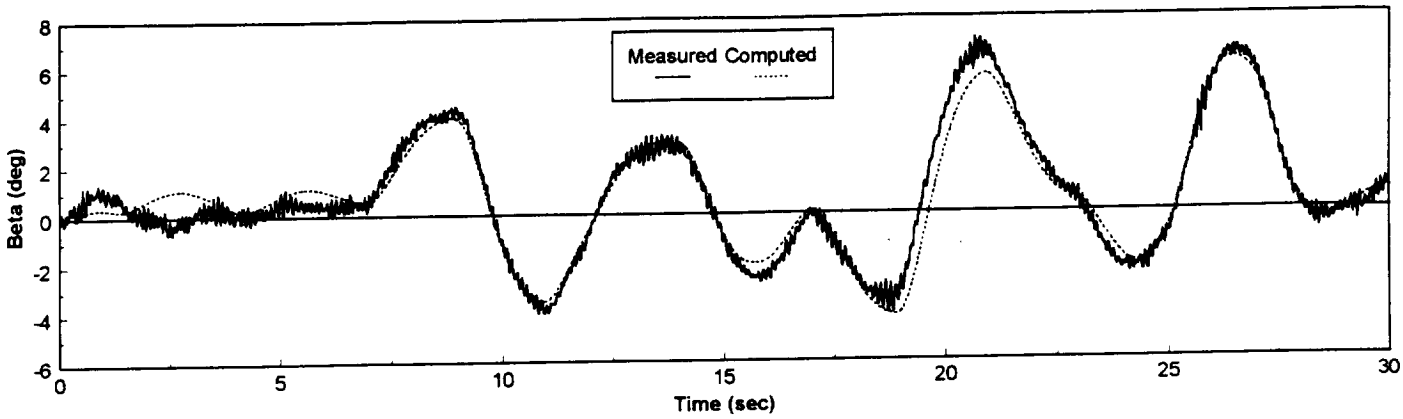

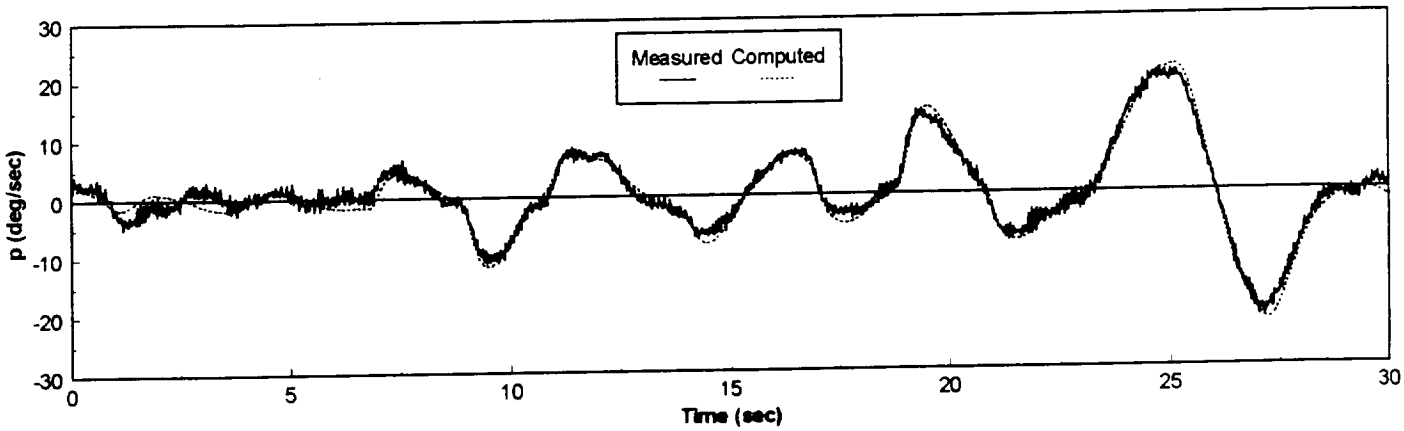

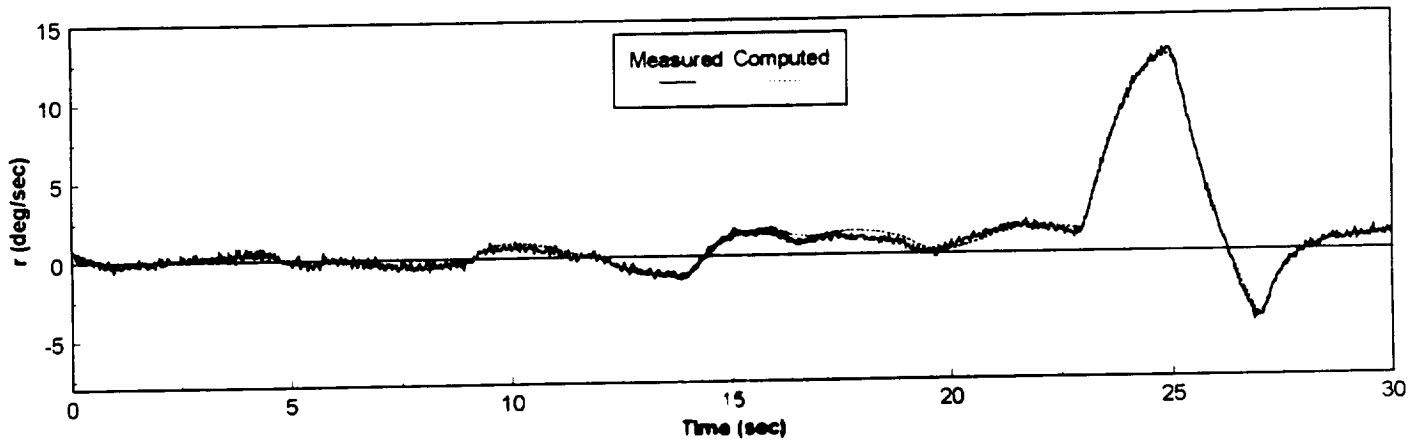

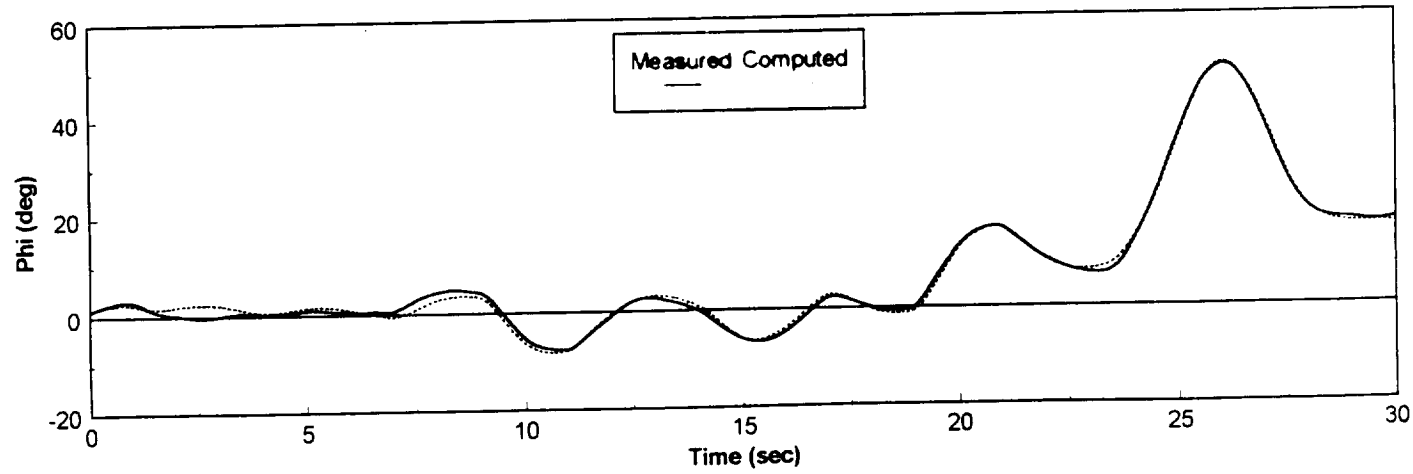

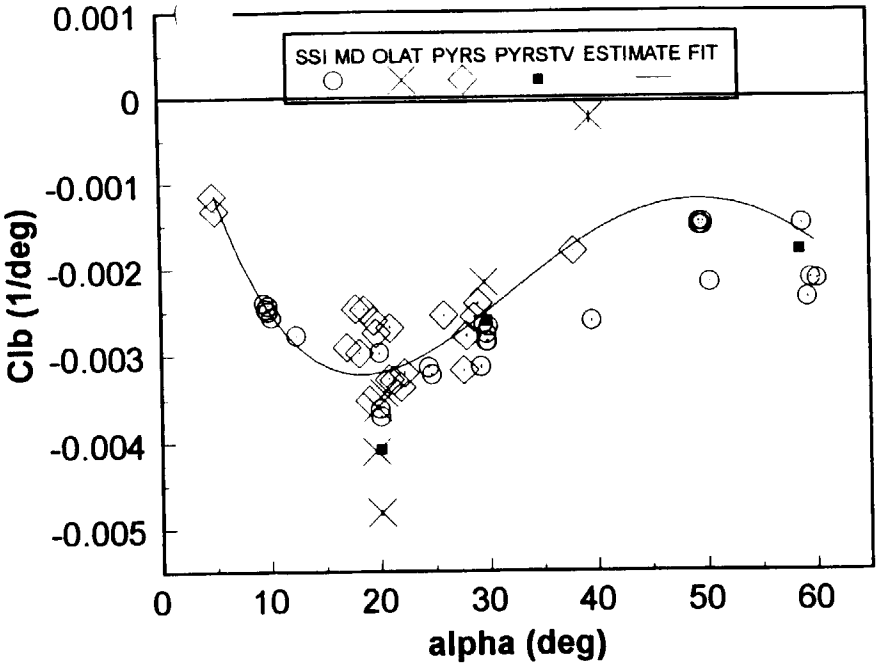
SSI MD OLAT PYRS PYRSTV ESTIMATE FIT
Clb (1/deg)
alpha (deg)
0.001
0
-0.001
-0.002
-0.003
-0.004
-0.005
0
10
20
30
40
50
60

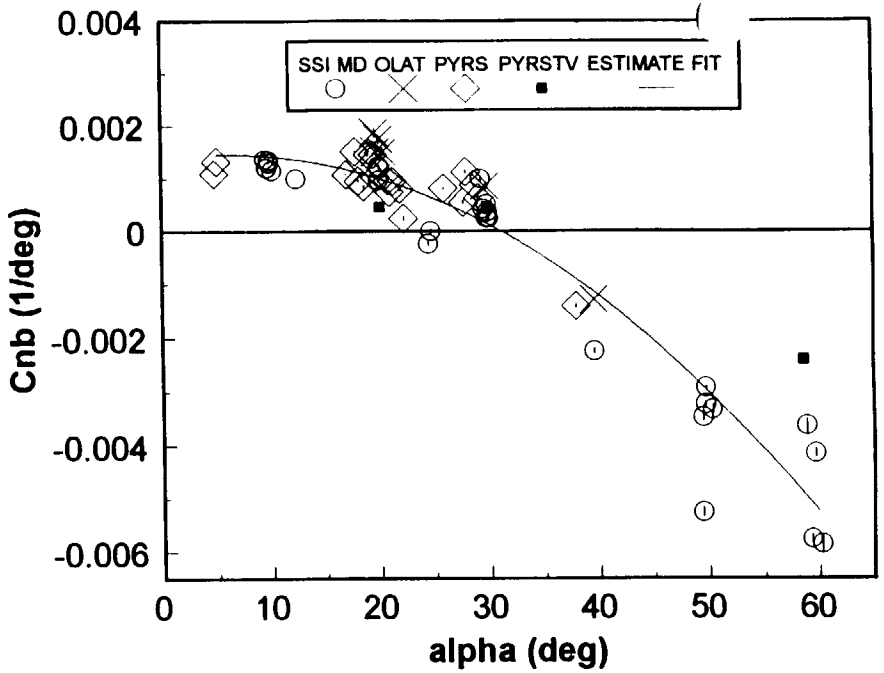
SSI MD OLAT PYRS PYRSTV ESTIMATE FIT
Cnb (1/deg)
alpha (deg)
0.004
0.002
0
-0.002
-0.004
-0.006
0
10
20
30
40
50
60

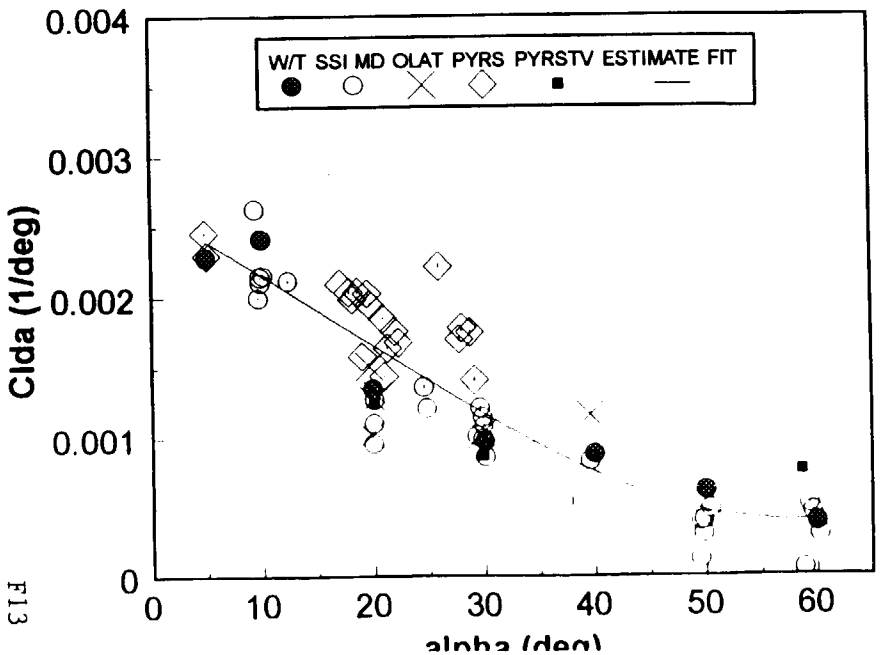
W/T SSI MD OLAT PYRS PYRSTV ESTIMATE FIT
Clda (1/deg)
alpha (deg)
0.004
0.003
0.002
0.001
0
0
10
20
30
40
50
60

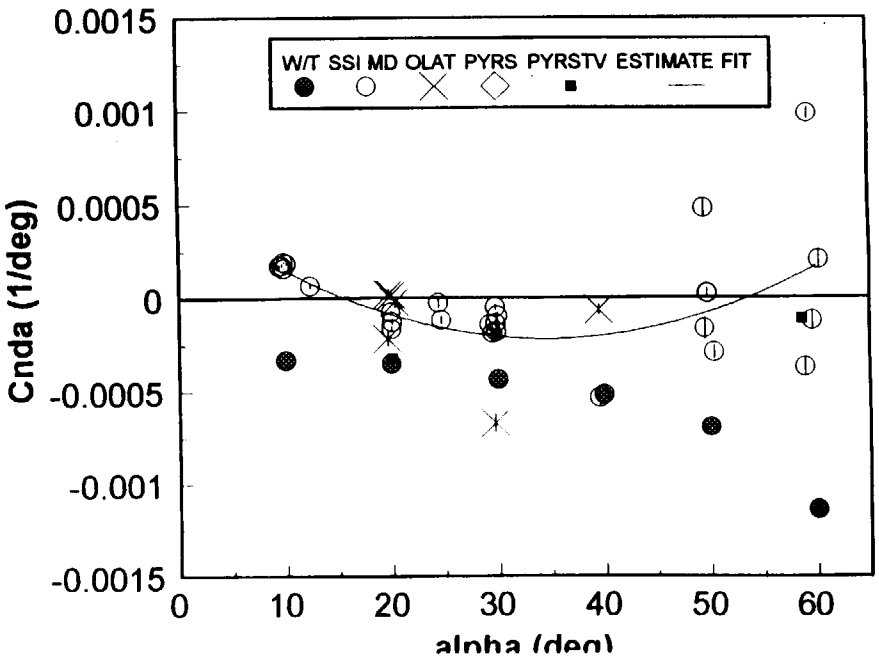
W/T SSI MD OLAT PYRS PYRSTV ESTIMATE FIT
Cnda (1/deg)
alpha (deg)
0.0015
0.001
0.0005
0
-0.0005
-0.001
-0.0015
0
10
20
30
40
50
60

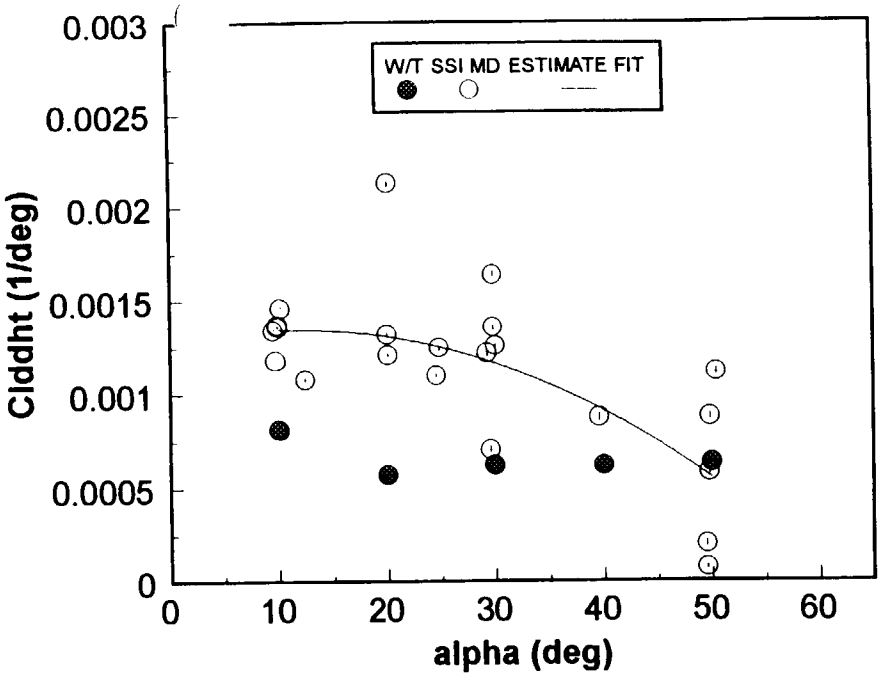
W/T SSI MD ESTIMATE FIT
Clddht (1/deg)
alpha (deg)
0.003
0.0025
0.002
0.0015
0.001
0.0005
0
0
10
20
30
40
50
60

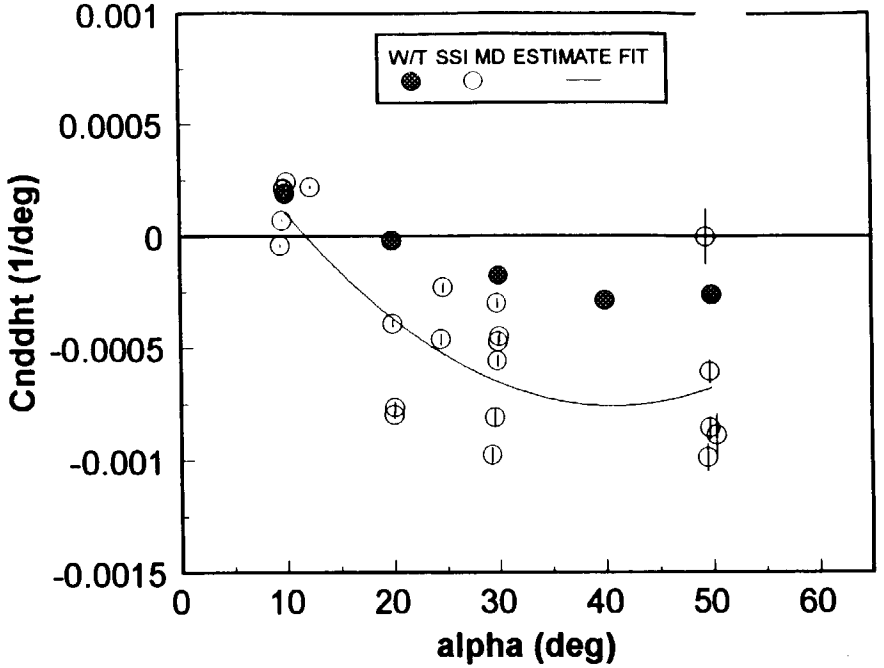
W/T SSI MD ESTIMATE FIT
Cnddht (1/deg)
alpha (deg)
0.001
0.0005
0
-0.0005
-0.001
-0.0015
0
10
20
30
40
50
60

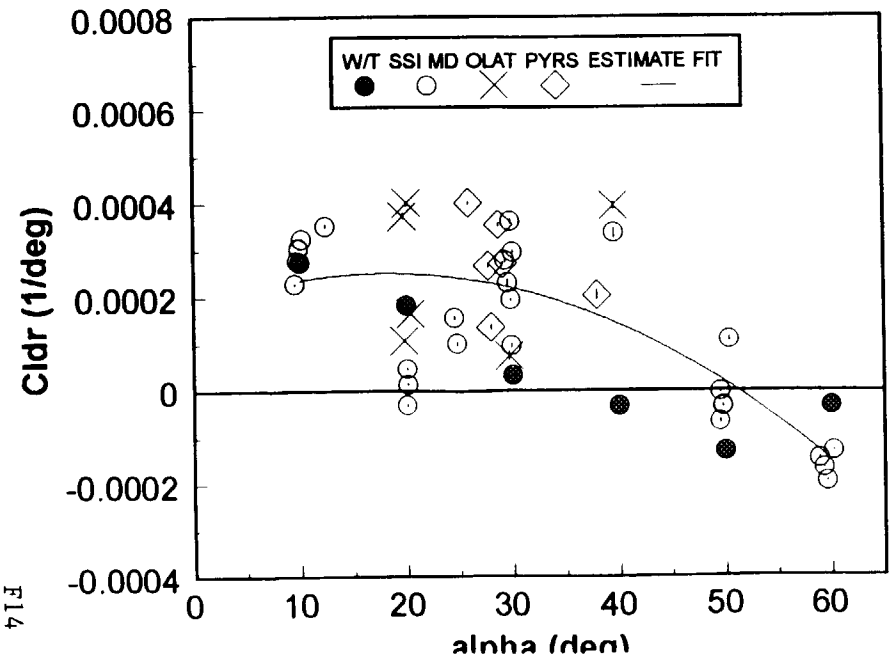
W/T SSI MD OLAT PYRS ESTIMATE FIT
Cldr (1/deg)
alpha (deg)
0.0008
0.0006
0.0004
0.0002
0
-0.0002
-0.0004
0
10
20
30
40
50
60

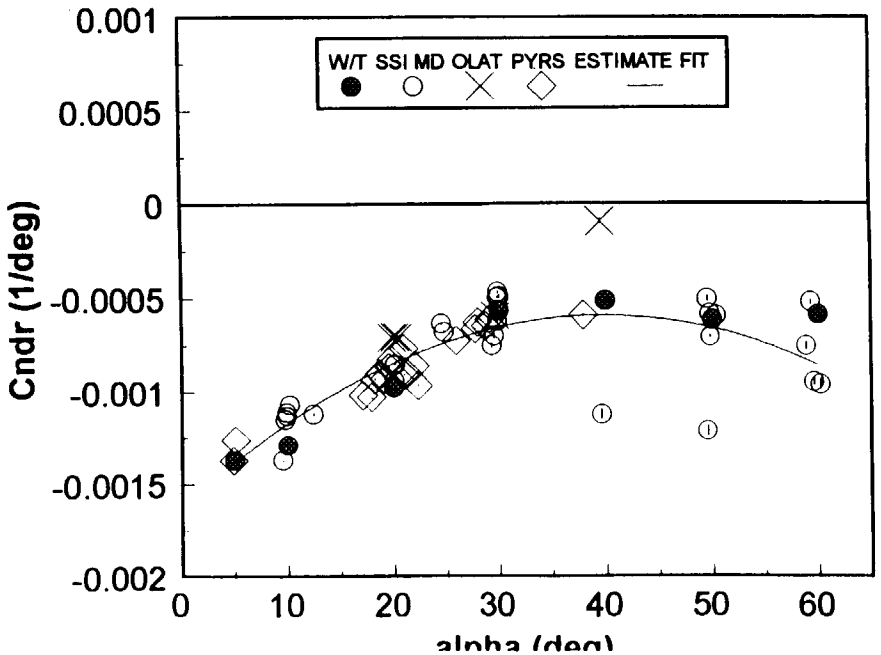
W/T SSI MD OLAT PYRS ESTIMATE FIT
Cndr (1/deg)
alpha (deg)
0.001
0.0005
0
-0.0005
-0.001
-0.0015
-0.002
0
10
20
30
40
50
60

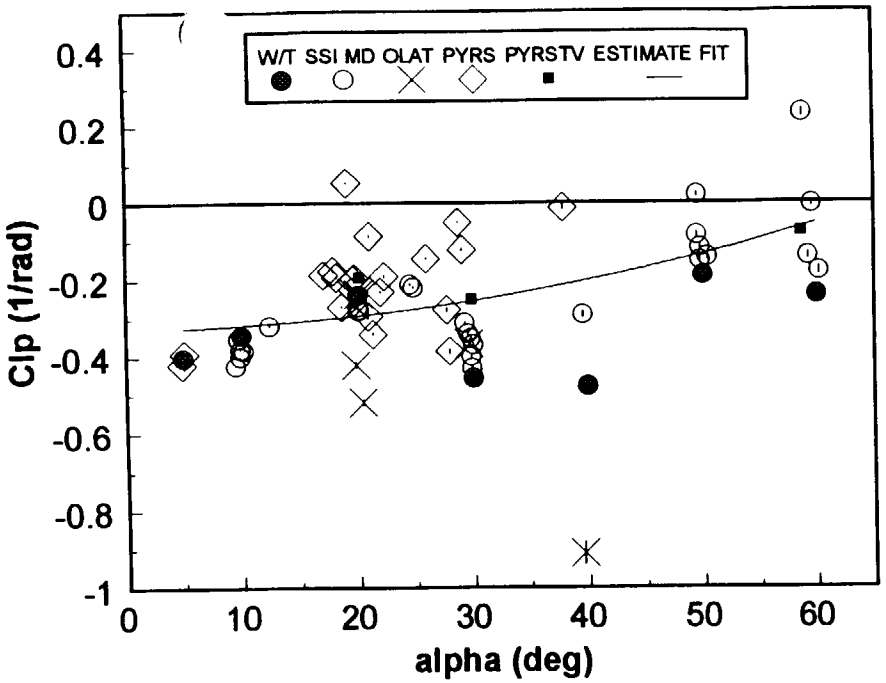
W/T SSI MD OLAT PYRS PYRSTV ESTIMATE FIT
Clp (1/rad)
alpha (deg)

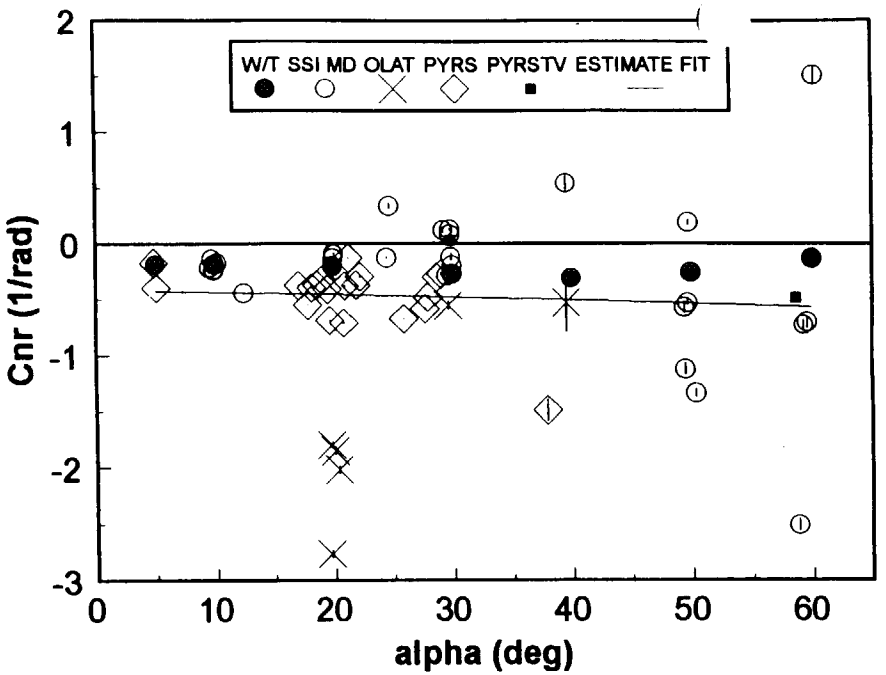
W/T SSI MD OLAT PYRS PYRSTV ESTIMATE FIT
Cnr (1/rad)
alpha (deg)

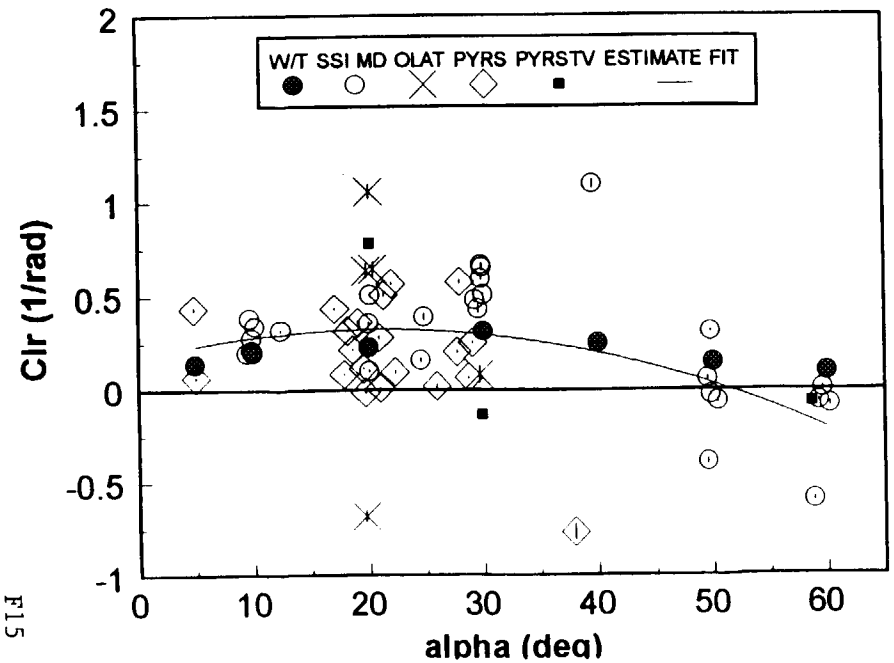
W/T SSI MD OLAT PYRS PYRSTV ESTIMATE FIT
Clr (1/rad)
alpha (deg)

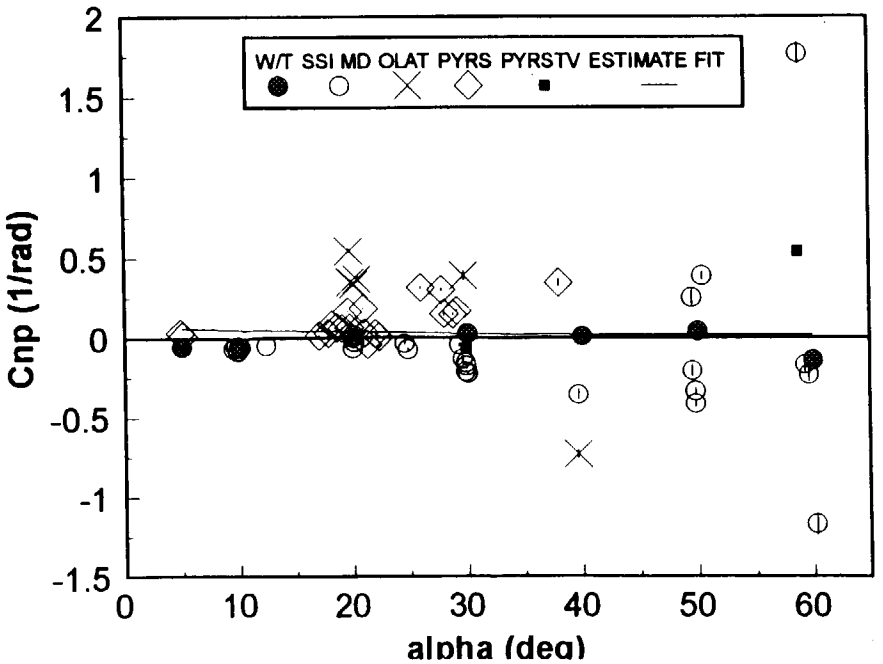
W/T SSI MD OLAT PYRS PYRSTV ESTIMATE FIT
Cnp (1/rad)
alpha (deg)

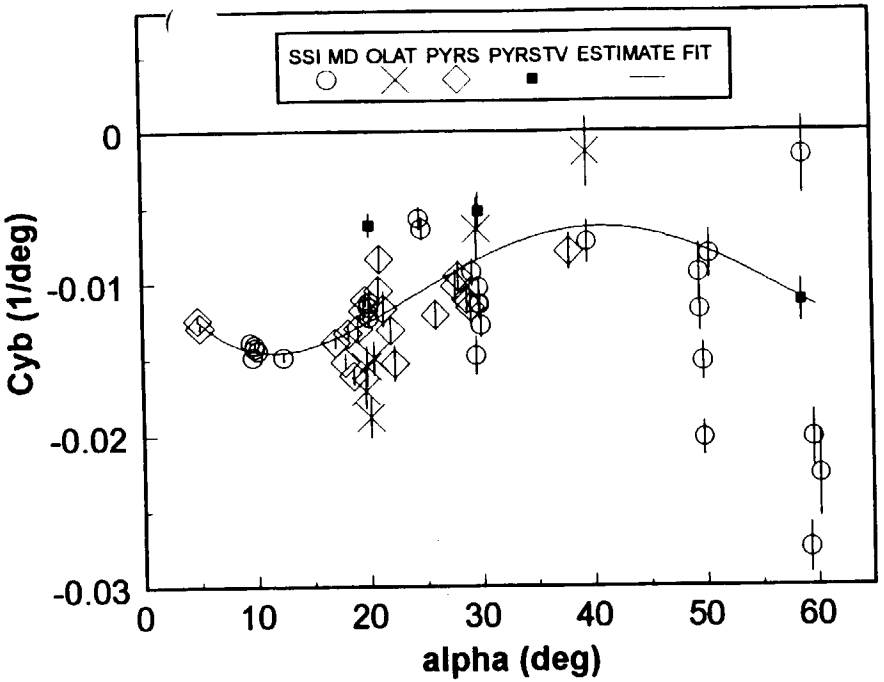
SSI MD OLAT PYRS PYRSTV ESTIMATE FIT
Cyb (1/deg)
0
-0.01
-0.02
-0.03
0
10
20
30
40
50
60
alpha (deg)

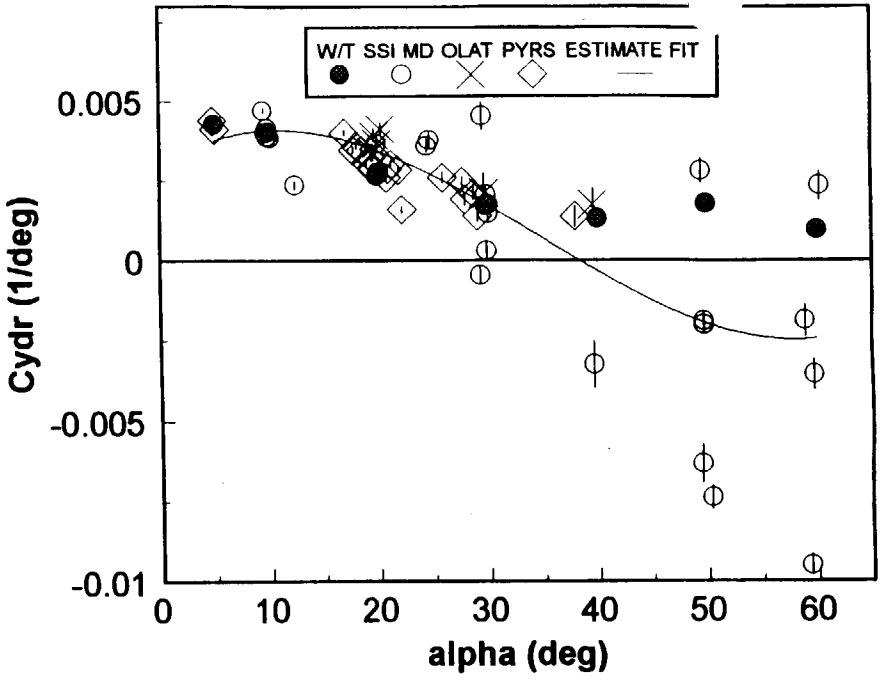
W/T SSI MD OLAT PYRS ESTIMATE FIT
Cydr (1/deg)
0.005
0
-0.005
-0.01
0
10
20
30
40
50
60
alpha (deg)

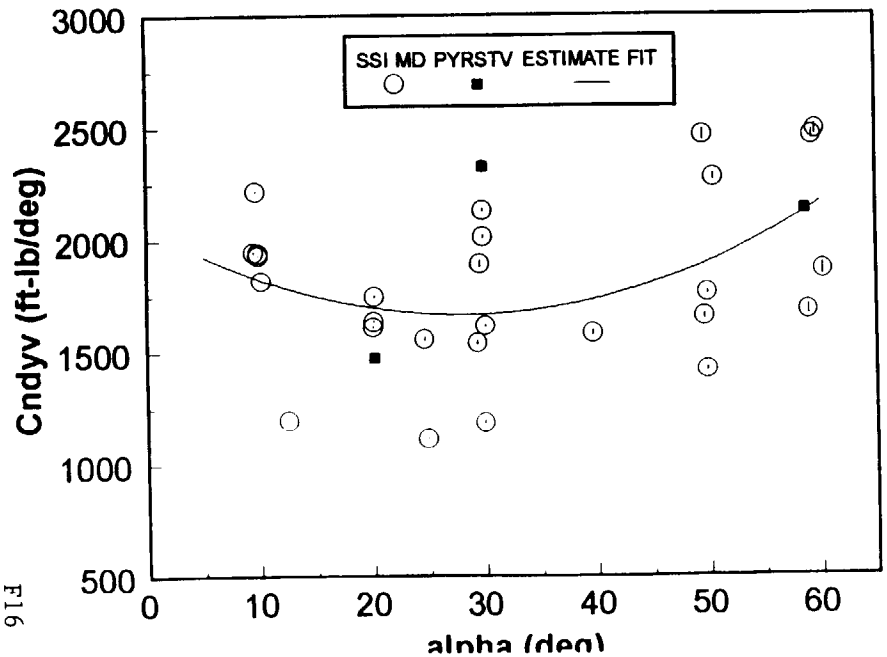
SSI MD PYRSTV ESTIMATE FIT
Cndyv (ft-lb/deg)
3000
2500
2000
1500
1000
500
0
10
20
30
40
50
60
alpha (deg)

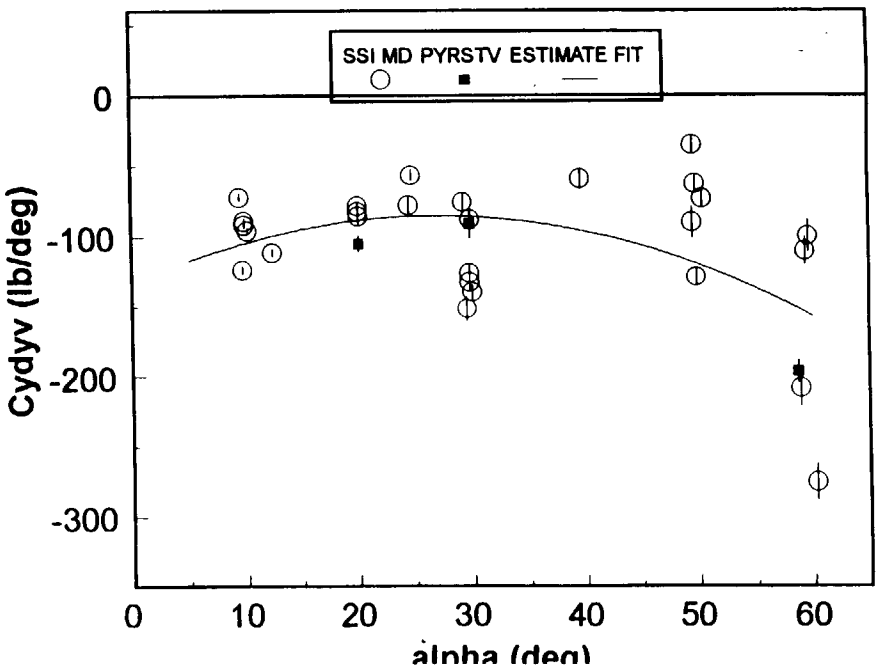
SSI MD PYRSTV ESTIMATE FIT
Cydyv (lb/deg)
0
-100
-200
-300
0
10
20
30
40
50
60
alpha (deg)